

Cumulant expansion framework for internal gradient distributions tensors

Leonardo A. Pedraza Pérez^{1,2} and Gonzalo A. Álvarez^{1,3,4,*}

¹*Instituto Balseiro, CNEA, Universidad Nacional de Cuyo, S. C. de Bariloche, 8400, Argentina.*

²*Centro Atómico Bariloche, CNEA, S. C. de Bariloche, 8400, Argentina.*

³*Centro Atómico Bariloche, CONICET, CNEA, S. C. de Bariloche, 8400, Argentina.*

⁴*Instituto de Nanociencia y Nanotecnología, CNEA, CONICET, S. C. de Bariloche, 8400, Argentina*

Magnetic resonance imaging is a powerful, non invasive tool for medical diagnosis. The low sensitivity for detecting the nuclear spin signals, typically limits the image resolution to several tens of micrometers in preclinical systems and millimeters in clinical scanners. Other sources of information, derived from diffusion processes of intrinsic molecules as water in the tissues, allow getting morphological information at micrometric and submicrometric scales as potential biomarkers of several pathologies. Here we consider extracting this morphological information by probing the distribution of internal magnetic field gradients induced by the heterogeneous magnetic susceptibility of the medium. We use a cumulants expansion to derive the dephasing on the spin signal induced by the molecules that explore these internal gradients while diffuse. Based on the cumulants expansion, we define internal gradient distributions tensors (IGDT) and propose modulating gradient spin echo sequences to probe them. These IGDT contain microstructural morphological information that characterize porous media and biological tissues. We evaluate the IGDT effects on the magnetization decay with typical conditions of brain tissue and show their effects can be experimentally observed. Our results thus provide a framework for exploiting IGDT as quantitative diagnostic tools.

1. INTRODUCTION

Magnetic resonance imaging (MRI) has proven to be a powerful technique for non-invasive medical diagnosis. The implementations of MRI techniques usually limit the spatial resolution to millimeters in clinical scanners and to tens of micrometers in preclinical systems. However, the monitored nuclear spins can probe smaller spatial scales. Different methods thus exploit various physical processes sensed by the nuclear spins such as molecular diffusion [1–21] or tissue properties as the magnetic susceptibility [22–31] to generate contrast that can unveil the tissue microstructure.

Based on these principles, diffusion-weighted images (DWI) display information about the motion of water molecules within tissues [32]. DWI has become a common diagnostic tool in clinical practice. For instance, the most established clinical indication for DWI is the assessment of cerebral ischemia [14]. DWI has been also used to monitor lesion aggressiveness and tumor response in oncology imaging [33]. Its extension to diffusion tensor imaging (DTI), based on estimating the components of the apparent diffusion coefficient along multiple directions, enables to determine tissue microstructure anisotropies which are very useful for tracking brain connectivity [34–39]. Nevertheless, there are cases where the anisotropy of the apparent diffusion tensor is small, as occurs in wide compartments or in fiber crossing regions in brain, and the application of DTI it is thus limited [37, 40–42].

Alternatively, susceptibility-weighted imaging (SWI) exploits the effect of tissues magnetic susceptibility

variations to generate high resolution (0.3 mm) anatomical images in high field scanners (>7 Tesla) [26]. Tissue susceptibility variations are encoded in the amplitude and phase of the magnetic resonance (MR) signal. Using this information it is possible to suppress or enhance spectral components and modify the contrast of different tissues. These concepts has been used for water/fat separation [43, 44], MR angiography [45–47] and gray/white-matter contrast [48]. Its application as disease biomarkers is highly encouraging for observing image changes based on iron and calcium concentration variations, and for axon demyelination [49–51]. However, to attain this quantitative information it is often required the rotation of the studied subject [52].

Biological tissues have very complex structures and compartmentalization heterogeneities due to different molecular compositions. Its intrinsic heterogeneity is imitated by magnetic susceptibility changes along the tissue structure [27, 30, 31, 53, 54]. In presence of an external magnetic field, the susceptibility discontinuities induce internal magnetic field gradients [22, 24, 25, 55–57]. These internal or background gradients are correlated with the pore size distribution, thus allowing the inference of tissue microstructure sizes from the internal gradients statistics [23, 28, 58–61]. Moreover, the internal gradient distributions contain also information about microstructure anisotropy, for example, related with fiber orientations [24, 30]. These techniques are specially useful when DTI fails due to almost isotropic diffusion scenarios. Importantly, compared with quantitative SWI, the statistical characterization of internal gradient distribution can be done without reorienting the subject with respect to the direction of the main magnetic field, thus allowing to extract anisotropic information based on susceptibility heterogeneities

* gonzalo.alvarez@cab.cnea.gov.ar

within tissues [24, 30].

Brain physiology is also regulated by an assemblage of molecules and structures as the myelin sheath of axons, with significant magnetic susceptibility changes with respect to the surrounding medium. The degree of axon myelination has been shown to significantly affect the transverse relaxation time and spin phases in white matter [25, 56]. Therefore, it is expected that internal gradient distributions also show correlation with the amount of myelin in such tissues [26, 29, 62, 63], thus being a potential biomarker of degenerative diseases.

In this article, we provide a perturbative framework to characterize and determine internal (or background) gradient distributions by its first statistical moments. These moments define internal gradient distributions tensors (IGDT) that provide information about the media anisotropy. We formalize previous works that evidence these IGDT [24, 30, 61, 63, 64], based on a cumulant expansion of the spin dephasing beyond a Gaussian phase approximation. We consider an internal gradient ensemble model, where spin-bearing molecules diffuse in presence of an effective gradient. This effective gradient is determined by the average gradient seen by the spin along the diffusion trajectory. This approach allows simplifying high order correlations of the spin displacement as the molecular diffusion can be considered a Gaussian process, and then write the magnetization signal with an IGDT expansion of different ranks. The IGDT may have subtle effects on the magnetization signal decay, thus we exploit the IGDT expansion to design Modulated Gradient Spin-Echo (MGSE) sequences [1, 32] that use cross-correlations between an applied and the internal gradient to enhance their contributions to the MR signal [30]. These MGSE sequences encode the internal gradient information on the diffusion weighting decay rather than on a phase-shift in the magnetization signal, as the latter is removed. We perform a combination of analytical and numerical analyses to demonstrate the feasibility of determining the IGDT in realistic conditions using typical brain tissue properties. We also discuss the validity of the proposed framework.

In Sec. 2 we describe the physical problem and the considered internal gradient ensemble model. Section 3 introduces the cumulant expansion framework for the magnetization decay and the derivation of the IGDT expansion. In Sec. 4 we propose a method for measuring the IGDT and design MGSE sequences to enhance the IGDT effects on the magnetization signal decay. Section 5 discusses the feasibility of measuring the IGDT for conditions similar to those founds in brain tissue. In Sec. 6 we discuss the scope and limitations of the considered model for characterizing the internal gradients. Finally, in Sec. 7 we summarize the results and elaborate some conclusions and outlook.

2. SPINS DIFFUSING IN AN INHOMOGENEOUS FIELD

2.1. Spin phase modulated by MGSE sequences and internal gradients

We consider an heterogeneous medium in presence of a static magnetic field \mathbf{B}_0 in the z direction. Due to inhomogeneities of the magnetic susceptibility in the sample, the effective magnetic field becomes also inhomogeneous leading to local field variations $\Delta B_0(\mathbf{x})$ depending on the spatial position \mathbf{x} . The typical magnetic field variations induced by the magnetic susceptibility changes in porous media are on the order of $\approx 10^{-6}\mathbf{B}_0$ [24, 32, 65, 66]. As these local field variations are significantly weaker than the static magnetic field strength, we only need to consider the z component of that local field, $\Delta B_0(\mathbf{x})$. Since $\Delta B_0(\mathbf{x})$ intrinsically depends on the microstructure morphology of the medium, we are interested to probe it to extract sub-voxel morphological information. As these field variations originate internal or background gradients $\mathbf{G}_0(\mathbf{x}) = \nabla\Delta B_0(\mathbf{x})$, with ∇ being the differential operator with respect to \mathbf{x} , they can be probed with the nuclear spin-bearing molecules diffusing within these internal field gradients [27, 30, 31, 65, 67–69].

The Brownian motion of spin-bearing particles in a constant magnetic field gradient induces spin dephasing that cannot be fully refocused by spin-echo based sequences [70–72]. This dephasing thus leads to a magnetization decay that is typically used to probe the molecular diffusion in porous media [32, 39, 73–75]. The temporal diffusion process can be characterized by applying magnetic field gradients that vary over time with a modulation function $f_G(t)$ [3, 5, 8, 76–78]. Thus, the phase acquired by a diffusing spin-bearing particle during a diffusion time t_d depends on the spin-bearing particle trajectory $\mathbf{x}(t)$, the internal field ΔB_0 and the applied gradient \mathbf{G} [24, 27, 30, 67–69, 74, 77] as

$$\phi[t_d, \mathbf{x}(t), \Delta B_0] = \gamma \int_0^{t_d} dt' \{ \mathbf{x}(t') \cdot \mathbf{G} f_G(t') + f_0(t') \Delta B_0[\mathbf{x}(t')] \}, \quad (1)$$

where γ is the gyromagnetic ratio of the nucleus.

The sign of the internal field can be controlled by radio-frequency (RF) π -pulses and it is described by the modulation function $f_0(t)$. The RF π -pulses globally affect the phase evolution of the spins. Each of these pulses effectively switch also the sign of the applied gradient in the toggling frame representation of the spins [27, 30]. The considered modulation $f_G(t)$ includes the effects of the total modulation due to the applied gradient control and the effective sign switches induced by the RF π -pulses. Thus, $f_G(t)$ denotes the effective modulation of the applied gradient interaction with the spins, see Fig. (1). Here we consider MGSE sequences [1, 32], where the

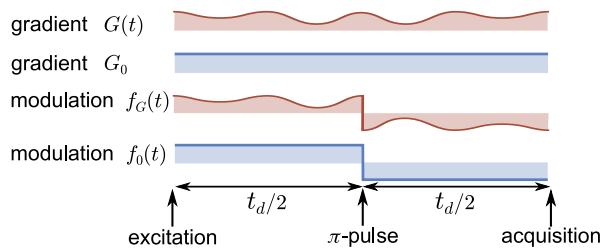


FIG. 1. Scheme for the effective applied gradient modulation function $f_G(t)$ and internal gradient modulation $f_0(t)$, based on an arbitrary applied gradient waveform $G(t)$ and a Hahn-echo sequence for modulating the internal gradient G_0 . The RF π -pulse of the Hahn-echo sequence induces a sign inversion of the applied and internal gradient modulations.

modulating functions satisfy

$$\int_0^{t_d} dt' f(t') = 0. \quad (2)$$

2.2. Internal Gradient ensemble model

An exact and rigorous treatment that describes the phase accumulation of Eq. (1) for a spin ensemble is in general very complex. We thus assume that the spin phase is characterized by an effective and spatially constant internal field gradient \mathbf{G}_0 during the diffusion time t_d (Fig. 2). Then, the spin phase is simplified to the form

$$\phi[t_d, \mathbf{x}(t), \mathbf{G}_0] = \gamma \int_0^{t_d} dt' \mathbf{x}(t') \cdot \{ \mathbf{G} f_G(t') + \mathbf{G}_0 f_0(t') \}. \quad (3)$$

The internal gradient \mathbf{G}_0 may be different for each particle depending on their position and diffusion pathway. We thus consider an ensemble of spin particles, and an ensemble of internal gradients [30, 63] leading to what we call the *internal gradient ensemble model* (Fig. 2).

The only relaxation mechanism of the spin phase that we consider here is the diffusion process in presence of magnetic field gradients. The total spin magnetization is given by the spin ensemble average that involves all possible realization of the spin's accumulated phase. Considering the introduced *internal gradient ensemble model*, the spin ensemble average is separated in the average of all possible fluctuating diffusion paths and the average over the distribution of the internal magnetic field gradients as

$$M(t_d) = \left\langle e^{i\phi[t_d, \mathbf{x}(t), \mathbf{G}_0]} \right\rangle_{\phi} = \left\langle e^{i\phi[t_d, \mathbf{x}(t), \mathbf{G}_0]} \right\rangle_{x, \mathbf{G}_0}. \quad (4)$$

Here, the brackets $\langle \cdot \rangle_{\phi}$ and $\langle \cdot \rangle_{x, \mathbf{G}_0}$ denote the ensemble average over the spin's accumulated phase, and the double average over the particle displacement paths

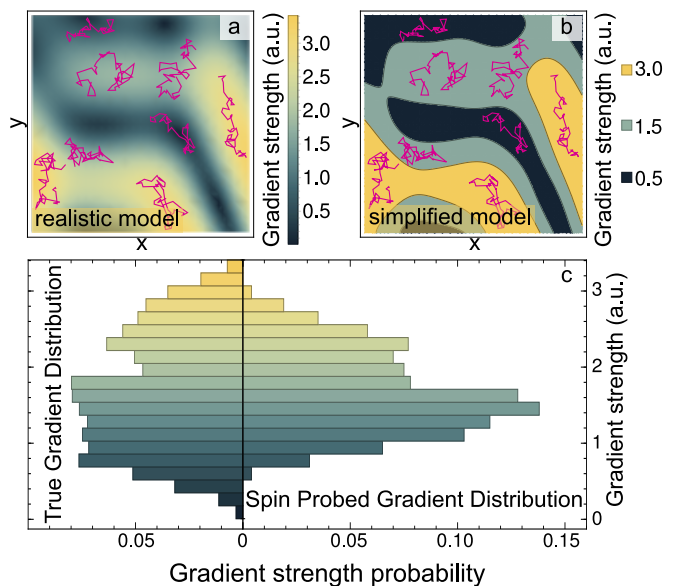


FIG. 2. Schematic representation of the internal gradient ensemble model. The internal gradient strengths are shown in colors represented in arbitrary units by the color bars. Realizations of the stochastic path of the Brownian motion of spin-bearing particles are shown with pink solid lines. (a) The gradient strength of a realistic model where a spin particle can diffuse freely in an inhomogeneous magnetic field. (b) Scheme for the simplified model where we assume a spin-bearing particle moves in a effective and constant gradient. (c) Comparison between the true gradient distribution associated to panel (a) and the effective gradient distribution probed by the diffusing spin-bearing particles schematized in (b). For the latter, we consider uniformly distributed spins that diffuse during a time t_d achieving a root mean square displacement $\sqrt{\langle (\mathbf{x}(t) - \langle \mathbf{x} \rangle)^2 \rangle}$ much lower than the boundary length of the simulation matrix. The constant gradient distribution mimics the true internal gradient distribution.

$\mathbf{x}(t)$ and the distribution of internal gradients \mathbf{G}_0 respectively. Figure 2 shows a schematic representation of these assumptions to describe the internal gradient distributions. A realistic model for single random realizations of spin-bearing particles moving freely within a space with internal gradient distributions is shown in Fig. 2a. Along the Brownian motion paths, the spins interact with different gradient strengths depending on their spatial position. Our simplified model for this motion is shown schematically in Fig. 2b, where we assume that, during the diffusion probing time t_d , a spin diffuses within a spatial region represented by an effective and constant magnetic field gradient. Then, the ensemble of constant gradient strengths considered in Eq. (4) accounts for the distribution of particles in the different gradient field strengths. Figure 2c shows how a realistic internal gradient distribution is mimicked by the one determined by the internal gradient ensemble model. Further considerations of the regimes where this gradient ensemble distribution can be used are discussed

in Sec. 6.

3. CUMULANT EXPANSION FRAMEWORK FOR INTERNAL GRADIENT DISTRIBUTIONS

3.1. Cumulant expansion for the spin dephasing

The fluctuating spin phase in presence of a constant gradient typically follows a Gaussian distribution [78–82]. However, due to the internal gradient distribution, the accumulated spin phase defined in Eq. (3) deviates from the Gaussian assumption. We thus determine the ensemble average of Eq. (4) by a cumulant expansion of the spin phase [83, 84]

$$\begin{aligned} \ln M(t_d) = & -\frac{1}{2} \langle\langle \phi(t_d)^2 \rangle\rangle + \frac{1}{4!} \langle\langle \phi(t_d)^4 \rangle\rangle \\ & - \frac{1}{6!} \langle\langle \phi(t_d)^6 \rangle\rangle + \dots \end{aligned} \quad (5)$$

Here, the double brackets $\langle\langle \phi^n \rangle\rangle$ denote the n th order cumulant for the random variable ϕ .

Following the internal gradient ensemble model introduced in Sec. 2.2, we separate the average of the spatial position due to the diffusion process from the average over the internal gradient distribution. The second order cumulant is thus

$$\begin{aligned} \langle\langle \phi(t_d)^2 \rangle\rangle = & \left\langle \Delta\phi [\mathbf{x}(t_d), \mathbf{G}_0]^2 \right\rangle_{x, G_0} \\ = & \beta_{ij}^{GG}(t_d) G_i G_j + \beta_{ij}^{00}(t_d) \langle \mathbf{G}_0 \mathbf{G}_0 \rangle_{ij} \\ & + 2\beta_{ij}^{0G}(t_d) G_i \langle \mathbf{G}_0 \rangle_j, \end{aligned} \quad (6)$$

where $\Delta\phi = \phi - \langle\phi\rangle$ is the deviation from the mean accumulated spin phase that we assume null $\langle\phi(t)\rangle = 0$, as the system is considered at the steady state under the application of MGSE sequences that satisfy Eq. (2). We use the Einstein sum convention in Eq. (6), where the indexes $i, j = x, y, z$ represent the three spatial directions. The averages $\langle \mathbf{G}_0 \rangle_j$ and $\langle \mathbf{G}_0 \mathbf{G}_0 \rangle_{ij}$ denote the matrix elements of the first two moments of the internal gradient distribution. The attenuation matrices

$$\begin{aligned} \beta^{GG}(t_d) = & \gamma^2 \int_0^{t_d} dt_1 \int_0^{t_d} dt_2 f_G(t_1) f_G(t_2) \\ & \times \langle \Delta\mathbf{x}(t_1) \Delta\mathbf{x}(t_2) \rangle \\ = & \gamma^2 \int_{-\infty}^{\infty} \frac{d\omega}{2\pi} |F_G(\omega, t_d)|^2 \mathbf{S}(\omega), \end{aligned} \quad (7)$$

$$\begin{aligned} \beta^{00}(t_d) = & \gamma^2 \int_0^{t_d} dt_1 \int_0^{t_d} dt_2 f_0(t_1) f_0(t_2) \\ & \times \langle \Delta\mathbf{x}(t_1) \Delta\mathbf{x}(t_2) \rangle \\ = & \gamma^2 \int_{-\infty}^{\infty} \frac{d\omega}{2\pi} |F_0(\omega, t_d)|^2 \mathbf{S}(\omega) \end{aligned} \quad (8)$$

and

$$\begin{aligned} \beta^{0G}(t_d) = & \gamma^2 \int_0^{t_d} dt_1 \int_0^{t_d} dt_2 f_0(t_1) f_G(t_2) \\ & \times \langle \Delta\mathbf{x}(t_1) \Delta\mathbf{x}(t_2) \rangle \\ = & \gamma^2 \int_{-\infty}^{\infty} \frac{d\omega}{2\pi} \Re [F_0(\omega, t_d) F_G^*(\omega, t_d)] \mathbf{S}(\omega) \end{aligned} \quad (9)$$

are overlap matrix functions that include all the temporal dependence of the magnetization decay. They are associated to the self-correlation tensor function of the spin displacement $\langle \Delta\mathbf{x}(t_1) \Delta\mathbf{x}(t_2) \rangle$ and to the gradient modulation functions $f_0(t)$ and $f_G(t)$. We consider modulation functions independent of the gradient direction. Here the instantaneous displacement $\Delta\mathbf{x}(t) = \mathbf{x}(t) - \langle \mathbf{x} \rangle$ is the deviation from its average value. These overlap matrix functions are also written in terms of their Fourier representations, where the Fourier transform of the gradient modulation functions is

$$F(\omega, t_d) = \int_0^{t_d} dt' e^{i\omega t'} f(t') \quad (10)$$

and, using the Wiener-Khinchin theorem, the displacement power spectrum matrix is

$$S_{ij}(\omega) = \int_{-\infty}^{\infty} dt' e^{i\omega t'} \langle \Delta x_i(t') \Delta x_j(0) \rangle, \quad (11)$$

assuming that the system is in the steady state.

The Fourier representation based on the displacement power spectrum defines the dephasing of the spin signal from the overlap between a filter function $|F(\omega, t)|^2$ that depends on the gradient control and the frequencies modes distribution of the diffusion process $\mathbf{S}(\omega)$ [3, 5, 8, 76–78]. Thus, the filter functions $|F(\omega, t)|^2$ can select what frequency component of the displacement power spectrum affects the dephasing.

Hence, the overlap matrix functions $\beta(t)$ can be tailored to probe the interaction of the diffusing spin-bearing particles with the modulated gradients [27, 30]. The matrices $\beta^{GG}(t)$ and $\beta^{00}(t)$ quantify the spin's interaction with the applied and background gradients respectively, and $\beta^{0G}(t)$ quantifies a cross-interaction of the spins with the applied and background gradients [30].

The next non-Gaussian correction of Eq. (5) is the 4th order cumulant $\langle\langle \phi(t_d)^4 \rangle\rangle$. This cumulant involves four time self-correlation tensor functions such as $\langle \Delta\mathbf{x}(t_1) \Delta\mathbf{x}(t_2) \Delta\mathbf{x}(t_3) \Delta\mathbf{x}(t_4) \rangle$, that can be simplified in terms of two times ones $\langle \Delta\mathbf{x}(t_1) \Delta\mathbf{x}(t_2) \rangle$ for Gaussian diffusion processes for the spin-bearing particle trajectory $\mathbf{x}(t)$.

3.2. Diffusion translation as a 3-dimensional Ornstein-Uhlenbeck process

According to the *internal gradient ensemble model*, the random variable describing the diffusion motion is

independent of the gradient distribution. Thus, to obtain analytical results we model the spin-bearing particles diffusion as a Gaussian and Markovian process according to the assumptions discussed below. This diffusion model allow us to simplify the high order self-correlation tensor function that appears in Eq. (5).

As typically assumed when modeling diffusion processes in restricted compartments, we require the diffusion propagator to be stationary when diffusion time tends to infinity. In one spatial dimension, the only Gaussian, Markovian and stationary process is the Ornstein-Uhlenbeck (OU) process [85, 86]. In the three-dimensional space, the OU process preserves these properties, therefore we consider this model of diffusion that allows analytical calculations.

In a general restricted media, the displacement correlation function along a given direction is given by

$$\langle \Delta x(0)\Delta x(t) \rangle = D_0 \sum_k b_k \tau_k e^{-|t|/\tau_k}, \quad (12)$$

where the coefficients b_k and characteristic times τ_k account for the specific geometry of the compartment [76, 87, 88]. Typically, the first of these exponential decays is the most significant, dominating the spin signal evolution [8, 78, 89]. The correlation function of the OU process is $\langle \Delta x(0)\Delta x(t) \rangle = D_0 \tau_c e^{-|t|/\tau_c}$ with the characteristic correlation time τ_c [8, 21, 78–80, 85, 89]. Thus, modeling the diffusion with an OU process is equivalent to approximate the correlation function of Eq. (12) to the one given by its dominant term.

Based on this assumption, the effective restriction length l_c of the microstructure compartment in which diffusion is taking place can be defined as the variance of the stationary displacement distribution of the OU process. This restriction length is defined by the correlation time through the equation $l_c^2 = D_0 \tau_c$ [32]. The restriction length l_c and the geometric size of the compartment depend on its shape. For the example of cylinders oriented perpendicular to the direction of the magnetic field gradient, a good approximation is $l_c = 0.37d$, where d is the cylinder diameter [3, 8, 76, 78].

The three-dimensional version of the OU process [90] accounts for anisotropic diffusion processes that are also typically found in porous media and biological tissues [35, 36, 38, 39, 91, 92]. In order to generate a quantitative model that introduces the microstructure morphology, we first consider that the free diffusion coefficient is isotropic leading to the tensor $\mathbf{D}_0 = D_0 \mathbf{I}$. The anisotropy of the diffusion process is thus only due to the compartment morphology. This anisotropy is introduced from the different correlation times along the different spatial directions in the displacement self-correlation tensor

$$\langle \Delta \mathbf{x}(t)\Delta \mathbf{x}(0) \rangle = D_0 \boldsymbol{\tau}_c \exp(-\boldsymbol{\tau}_c^{-1} |t|). \quad (13)$$

Here the correlation-time tensor $\boldsymbol{\tau}_c$ has as eigenvalues the diffusion correlation times τ_i along the principal axes of the compartment geometry (Fig. 3). The Fourier

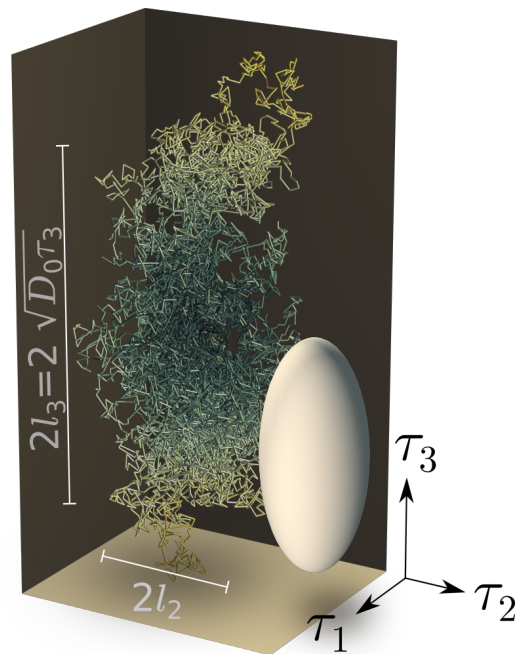


FIG. 3. Schematic representation of anisotropic diffusion due to anisotropic restriction lengths. The spin trajectory in space is restricted, described by a OU stochastic process with restriction lengths $l_3 > l_2 = l_1$, where $l_i^2 = D_0 \tau_i$. The ellipsoid represents the corresponding correlation time tensor $\boldsymbol{\tau}_c$.

transform of displacement self-correlation tensor gives the three-dimensional displacement power spectrum

$$\mathbf{S}(\boldsymbol{\omega}) = 2D_0 (\boldsymbol{\tau}_c^{-2} + \mathbf{I}\boldsymbol{\omega}^2)^{-1}. \quad (14)$$

Thus the anisotropy in the displacement power spectrum tensor reflects directly the anisotropy of the microstructure compartment morphology. In the following, we calculate the overlap matrix functions of Eqs. (7-9) based on this diffusion model.

3.3. The IGDT expansion

We consider the cumulant expansion up to the first non-Gaussian correction, that is up to the 4th order cumulant of Eq. (5) and thus assume the diffusion process for the spin-bearing particle is driven by an OU process. The non-Gaussian effects increase with the internal gradient variance $\langle \Delta G_0^2 \rangle$, where $\Delta \mathbf{G}_0 = \mathbf{G}_0 - \langle \mathbf{G}_0 \rangle$. It is thus expected the expansion of Eq. (5) to work well if $\|\mathbf{G} + \langle \mathbf{G}_0 \rangle\| \gg \sqrt{\langle \Delta G_0^2 \rangle}$. Therefore, we rewrite Eq. (5) in term of the moments of the internal gradient distribution. In general, the cumulant expansion (5) converges slowly and irregularly with the addition of higher order terms [75]. Then, to improve the convergence of the expansion up to the 4th order cumulant, we omit the internal gradient

distribution moments of order higher than 3. Under these assumptions, the magnetization decay is

$$\begin{aligned}
\ln M(t_d) = & -\frac{1}{2}G_i\beta_{ij}^{GG}(t_d)G_j - G_i\beta_{ij}^{0G}(t_d)\langle\mathbf{G}_0\rangle_j \\
& -\frac{1}{2}\beta_{ij}^{00}(t_d)\langle\mathbf{G}_0\mathbf{G}_0\rangle_{ij} \\
& +\frac{1}{2}G_iG_l\beta_{ij}^{0G}(t_d)\beta_{lk}^{0G}(t_d)\langle\Delta\mathbf{G}_0\Delta\mathbf{G}_0\rangle_{jk} \\
& +G_i\beta_{ij}^{0G}(t_d)\beta_{lk}^{00}(t_d)\langle\mathbf{G}_0\rangle_l\langle\Delta\mathbf{G}_0\Delta\mathbf{G}_0\rangle_{jk} \\
& +\frac{1}{2}\beta_{ij}^{00}(t_d)\beta_{kl}^{00}(t_d)\langle\mathbf{G}_0\rangle_i\langle\mathbf{G}_0\rangle_l\langle\Delta\mathbf{G}_0\Delta\mathbf{G}_0\rangle_{jkl} \\
& +\frac{1}{2}G_i\beta_{ij}^{0G}(t_d)\beta_{lk}^{00}(t_d)\langle\Delta\mathbf{G}_0\Delta\mathbf{G}_0\Delta\mathbf{G}_0\rangle_{jkl} \\
& +\frac{1}{2}\beta_{ij}^{00}(t_d)\beta_{lk}^{00}(t_d)\langle\mathbf{G}_0\rangle_i\langle\Delta\mathbf{G}_0\Delta\mathbf{G}_0\Delta\mathbf{G}_0\rangle_{jkl} \\
& +\mathcal{O}[\langle\Delta\mathbf{G}_0^4\rangle], \tag{15}
\end{aligned}$$

where we used the Einstein notation again. The moments $\langle\mathbf{G}_0\mathbf{G}_0\cdots\rangle_{ij\dots}$ and the central moments $\langle\Delta\mathbf{G}_0\Delta\mathbf{G}_0\cdots\rangle_{ij\dots}$ denote the matrix elements of the IGDT. Notice that the average is taken over the internal gradient distribution, expressing the cumulant expansion of Eq. (5) in terms of the IGDT of different ranks.

The expansion of Eq. (15) involves several terms that depend on the applied gradient strength G and the IGDT of different ranks, combined with the overlap integrals between gradient modulation functions and the displacement self-correlations given by the matrices $\beta^{GG}(t)$, $\beta^{00}(t)$ and $\beta^{0G}(t)$. Equation (15) thus sets one of the main results of this article, defining what we call the *IGDT-expansion*. Table I summarize the notation we use in the following for all the terms of Eq. (15).

The leading term $\chi_{G^2} = -\frac{1}{2}G_i\beta_{ij}^{GG}(t_d)G_j$ only depends on the applied gradient modulation. The next term $\chi_{0G} = -G_i\beta_{ij}^{0G}(t_d)\langle\mathbf{G}_0\rangle_j$ is a *cross-term* involving the overlap integral of the displacement power spectrum with the applied and internal gradient modulation filters. The overlap matrix $\beta^{0G}(t)$ can be positive, negative or null depending on the gradient modulation shapes and symmetries, unlike the attenuation matrices $\beta^{GG}(t)$ and $\beta^{00}(t)$ that are always positive defined. The magnitude of χ_{0G} depends on the angle between the applied gradient and the internal gradient, therefore it can be controlled by the applied gradient direction to probe the internal gradient direction. Accordingly, its sign depends on the direction of \mathbf{G} . The next term $\chi_{0^2} = -\frac{1}{2}\beta_{ij}^{00}(t_d)\langle\mathbf{G}_0\mathbf{G}_0\rangle_{ij}$ is proportional to the mean square value of the background gradient, but it is insensitive to its spatial orientation.

The next relevant term is $\chi_{G^2\Delta^2} = \frac{1}{2}G_iG_l\beta_{ij}^{0G}(t_d)\beta_{kl}^{0G}(t_d)\langle\Delta\mathbf{G}_0\Delta\mathbf{G}_0\rangle_{jk}$. This is also a *cross-term* similarly to χ_{0G} , but it involves the variance IGDT $\langle\Delta\mathbf{G}_0\Delta\mathbf{G}_0\rangle$. This variance tensor provides information about the anisotropy of the internal gradient distribution widths along the different spatial directions, and thus depends on the media morphology [30]. Then, the term $\chi_{0^2\Delta^2} = \frac{1}{2}\beta_{ij}^{00}(t_d)\beta_{kl}^{00}(t_d)\langle\mathbf{G}_0\rangle_i\langle\mathbf{G}_0\rangle_l\langle\Delta\mathbf{G}_0\Delta\mathbf{G}_0\rangle_{jkl}$

depends only on the internal gradient and contains information about its distribution width. However, it is invariant under applied gradient modulations, thus it does not provide information about internal gradient anisotropy. The term $\chi_{0G\Delta^2} = G_i\beta_{ij}^{0G}(t_d)\beta_{kl}^{00}(t_d)\langle\mathbf{G}_0\rangle_l\langle\Delta\mathbf{G}_0\Delta\mathbf{G}_0\rangle_{jk}$ is a *cross-term* as $\chi_{G^2\Delta^2}$ and χ_{0G} , and in this case its magnitude can be controlled by the applied gradient. By suitable control of the symmetries of the gradient's modulations it may vanish. Moreover, the sign of $\chi_{0G\Delta^2}$ changes also like χ_{0G} when the direction of the applied gradient is inverted. The last two terms $\chi_{G\Delta^3} = \frac{1}{2}G_i\beta_{ij}^{0G}(t_d)\beta_{kl}^{00}(t_d)\langle\Delta\mathbf{G}_0\Delta\mathbf{G}_0\Delta\mathbf{G}_0\rangle_{jkl}$ and $\chi_{0\Delta^3} = \frac{1}{2}\beta_{ij}^{00}(t_d)\beta_{kl}^{00}(t_d)\langle\mathbf{G}_0\rangle_i\langle\Delta\mathbf{G}_0\Delta\mathbf{G}_0\Delta\mathbf{G}_0\rangle_{jkl}$, involve IGDT tensors of the 3th order that give information about the skewness of the internal gradient distribution. They thus vanish for symmetric distributions.

4. DISTILLING AND IMPROVING THE IGDT EXPANSION EFFECTS ON THE SPIN DEPHASING

4.1. Observing IGDT terms

We aim at distilling the contribution of the different IGDT-expansion terms in Eq. (15) and maximizing their effects on the spin magnetization decay. We use MGSE sequences to avoid a phase shift induced by the mean macroscopic inhomogeneity in the magnetization signal according to Eq. (2) [27]. We then identify four groups of terms in the IGDT-expansion $\ln M = \chi_{\text{app}} + \chi_{\text{bck}} + \chi_{\text{odd-cross}} + \chi_{\text{even-cross}}$ of Eq. (15) (see Table I):

- (i) *the pure applied term* $\chi_{\text{app}} = \chi_{G^2}$;
- (ii) *the pure background terms:* $\chi_{\text{bck}} = \chi_{0^2} + \chi_{0^2\Delta^2} + \chi_{0\Delta^3}$;
- (iii) *the odd cross-terms* $\chi_{\text{odd-cross}} = \chi_{0G} + \chi_{0G\Delta^2} + \chi_{G\Delta^3}$;
- (iv) *and the even cross-term* $\chi_{\text{even-cross}} = \chi_{G^2\Delta^2}$.

These terms can be probed selectively by suitable design of the gradient modulation sequence inspired on a previous proposal [30]. We can observe directly *the pure applied* and *background* gradient terms (i and ii) $\chi_{\text{app}} + \chi_{\text{bck}}$, by making null *the cross-terms* contribution described in (iii) and (iv). *The cross-terms* are null if the overlap matrix $\beta^{0G}(t_d) = 0$, by generating an odd function for the product $f_0(t)f_G(t)$ with respect to the diffusion time $t_d/2$. This is done by exploiting the symmetries of applied and background gradient modulation to generate what we call the *symmetric sequence* as shown in Fig. 4a. Thus, the magnetization attenuation factor for this sequence is $\ln M_{\text{Sym}} = \chi_{\text{app}} + \chi_{\text{bck}}$. The *pure background* gradient effects (ii) can be selectively observed by a null applied gradient, *i.e.* we

IGDT groups	IGDT names	Definition	Description of the IGDT term
χ_{app}	χ_{G^2}	$-\frac{1}{2}G_i\beta_{ij}^{GG}(t)G_j$	Applied gradient weighting
χ_{bck}	χ_{0^2}	$-\frac{1}{2}\beta_{ij}^{00}(t)\langle\mathbf{G}_0\mathbf{G}_0\rangle_{ij}$	Trace-weighting of the internal gradient variance tensor
	$\chi_{0^2\Delta^2}$	$\frac{1}{2}\beta_{ij}^{00}(t)\beta_{kl}^{00}(t)\langle\mathbf{G}_0\rangle_i\langle\mathbf{G}_0\rangle_l\langle\Delta\mathbf{G}_0\Delta\mathbf{G}_0\rangle_{jk}$	Weighting of the internal gradient variance tensor in the mean internal gradient direction
	$\chi_{0\Delta^3}$	$\frac{1}{2}\beta_{ij}^{00}(t)\beta_{kl}^{00}(t)\langle\mathbf{G}_0\rangle_i\langle\Delta\mathbf{G}_0\Delta\mathbf{G}_0\Delta\mathbf{G}_0\rangle_{jkl}$	Weighting of the internal gradient distribution skewness
$\chi_{\text{odd-cross}}$	χ_{0G}	$-G_i\beta_{ij}^{0G}(t)\langle\mathbf{G}_0\rangle_j$	Weighting of the internal mean gradient projected into the applied gradient direction
	$\chi_{0G\Delta^2}$	$G_i\beta_{ij}^{0G}(t)\beta_{kl}^{00}(t)\langle\mathbf{G}_0\rangle_l\langle\Delta\mathbf{G}_0\Delta\mathbf{G}_0\rangle_{jk}$	Weighting of the internal gradient variance tensor projected in the applied and internal mean gradient directions
	$\chi_{G\Delta^3}$	$\frac{1}{2}G_i\beta_{ij}^{0G}(t)\beta_{kl}^{00}(t)\langle\Delta\mathbf{G}_0\Delta\mathbf{G}_0\Delta\mathbf{G}_0\rangle_{jkl}$	Cross-weighting of the internal gradient distribution skewness with the applied gradient
$\chi_{\text{even-cross}}$	$\chi_{G^2\Delta^2}$	$\frac{1}{2}G_iG_l\beta_{ij}^{0G}(t)\beta_{kl}^{0G}(t)\langle\Delta\mathbf{G}_0\Delta\mathbf{G}_0\rangle_{jk}$	Internal gradient variance tensor weighted in the applied gradient direction

TABLE I. Nomenclature for the different IGDT terms of the cumulant expansion, their definitions and physical description. The term descriptions in the last column give geometric interpretation assuming isotropic diffusion, *i.e.* overlap matrices $\beta(t)$ proportional to the identity. The more general interpretation is based on considering the overlap matrices as metric tensors that modify the inner product of the gradient vectors. In this case the overlap matrices $\beta^{GG}(t)$ and $\beta^{00}(t)$ are real, symmetric and positive-definite while $\beta^{0G}(t)$ may be null, negative or positive-definite depending on the gradient modulation symmetries. Given a non-singular symmetric matrix β , we can define an inner product (\cdot, \cdot) between two vectors \mathbf{u} and \mathbf{v} as $(\mathbf{u}, \mathbf{v}) = \mathbf{u} \cdot \beta \cdot \mathbf{v}$. Here β is the metric tensor and is a generalization of the traditional Euclidean inner product $\mathbf{u} \cdot \mathbf{v} = \mathbf{u} \cdot \mathbf{I} \cdot \mathbf{v}$. The definitions in the third column can be interpreted by this inner product generalization with a metric defined by the anisotropy of the diffusion process encoded by the β matrices.

obtain $\ln M_{\text{Sym}, \mathbf{G}=0} = \chi_{\text{bck}}$. Then by subtracting its corresponding attenuation factor to the one obtained by the *symmetric sequence*, we can probe *the pure applied* gradient terms $\chi_{\text{app}} = \ln M_{\text{Sym}} - \ln M_{\text{Sym}, \mathbf{G}=0}$.

We then increase the cross overlap matrix $\beta^{0G}(t_d)$ contribution while keeping invariant $\beta^{GG}(t_d)$ and $\beta^{00}(t_d)$. This is done by only relatively shifting the applied and background gradient modulations functions, creating what we call an *asymmetric sequence* as shown in Fig. 4b. Thus, by subtracting the attenuation factors from the decaying signals between the *symmetric* and *asymmetric sequences*, we can selectively observe the *cross-terms* contributions $\chi_{\text{odd-cross}} + \chi_{\text{even-cross}} = \ln M_{\text{Asym}} - \ln M_{\text{Sym}}$. We then exploit the fact that the *odd cross-terms* change their sign by inverting the applied gradient direction, while *the even cross-terms* are invariant against this change. Again, by subtracting or adding the attenuation factors derived from the inverted directions of the applied gradient we can selectively probe *the odd cross-terms*

$$\chi_{\text{odd-cross}} = 1/2 \ln M_{\text{Asym}, +\mathbf{G}} - 1/2 \ln M_{\text{Asym}, -\mathbf{G}} \quad (16)$$

and *the even cross-term*

$$\chi_{\text{even-cross}} = 1/2 \ln M_{\text{Asym}, +\mathbf{G}} + 1/2 \ln M_{\text{Asym}, -\mathbf{G}} - \ln M_{\text{Sym}}. \quad (17)$$

Figure 4c shows a scheme manifesting the described signal behaviors.

For a 3-dimensional IGDT inference, we must repeat this strategy on multiple non-collinear applied gradient

directions in order to determine the IGDT terms. Inspired on the methods for reconstructing the diffusion tensor [35, 36], we proposed a technique to extract $\langle\mathbf{G}_0\rangle$ and $\langle\Delta\mathbf{G}_0\Delta\mathbf{G}_0\rangle$ in Ref. [30]. First, we need to determine the pure applied gradient overlap matrix $\beta^{GG}(t)$ to find the correlation-time tensor τ_c and the free diffusion coefficient D_0 . The matrix $\beta^{GG}(t)$ has six independent elements. Therefore, we must measure *the pure applied term* χ_{app} at least for six non-collinear applied gradient directions. As the attenuation terms are noisy, it is also important to increase the number of non-collinear gradient directions [37, 40, 93] to estimate $\beta^{GG}(t)$ statistically using a multivariate linear regression. The correlation times in each direction and the free diffusion coefficient can be estimated by fitting the estimated $\beta^{GG}(t)$ based on our analytic model (7).

Once these parameters are determined, we can calculate the other two overlap matrices $\beta^{0G}(t)$ and $\beta^{00}(t)$ in term of them using Eqs. (8), (9) and (14). With the overlap matrix $\beta^{0G}(t)$ reconstructed, we can estimate the IGDT $\langle\Delta\mathbf{G}_0\Delta\mathbf{G}_0\rangle$ and the mean internal gradient vector $\langle\mathbf{G}_0\rangle$ by measuring *the even cross-term* $\chi_{\text{even-cross}}$ and *the odd cross-terms* $\chi_{\text{odd-cross}}$ at several applied gradient directions and using the multivariate linear regression.

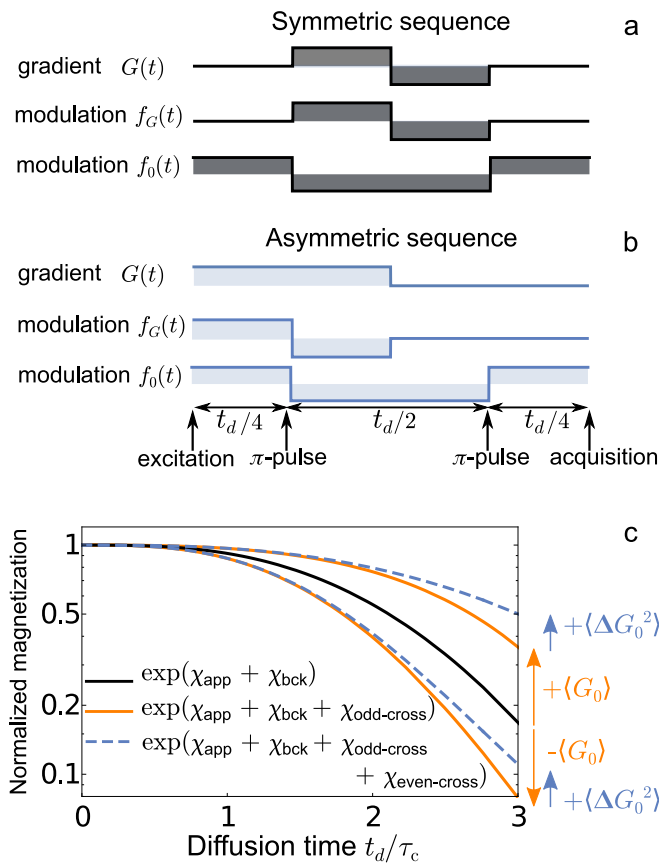


FIG. 4. Schematic representation of a *symmetric* (a), an *asymmetric sequence* (b) and the corresponding spin signals behavior based on the contribution of the different IGDT terms (c). The solid black line in (c) corresponds to the attenuation induced by the pure applied (i) and pure background gradients (ii) terms derived from the symmetric sequence. The orange solid lines add the *odd cross-terms* contributions (iii) to the signal attenuation. Depending on the relative direction between the applied and mean background gradient, this contribution is positive or negative. The blue dashed lines in (c) are the signal decay derived from the asymmetric sequence, that add the *even cross-term* contribution, which is proportional to the covariance tensor of the internal gradient distribution. The *even-cross terms* are always positive independent on the applied gradient direction.

4.2. Sequence design to enhance the IGDT contributions

The IGDT contributions may be weak. Due to the overlap matrix $\beta^{0G}(t_d)$ appears as a dyadic product in the *cross-terms* $\chi_{G^2\Delta^2}$, $\chi_{0G\Delta^2}$ and $\chi_{0^2\Delta^2}$, they become more relevant than the *pure applied* and *pure background gradient* ones as the diffusion time increases. This can be seen by considering the asymptotic behavior of the attenuation factors $\beta(t_d) \sim 2c\gamma^2 D_0 \tau_c^2 t_d$ and $\beta(t_d) \sim 2c\gamma^2 D_0 t_d^3$, for the restricted ($t_d \gg \tau_c$) and free ($t_d \ll \tau_c$) diffusion limits, respectively. Here c is a dimensionless coefficient that depends on the specific

gradient modulation waveform. The first order terms that are linearly proportional to the overlap matrices $\beta(t_d)$ are the most significant on the attenuation factor up to the following approximated time scale

$$t_{G_{tot}} = \left[c\gamma^2 D_0 (\mathbf{G} + \langle \mathbf{G}_0 \rangle)^2 \right]^{-1/3}, \quad (18)$$

for the free diffusion regime and

$$t_{G_{tot}} = \left[c\gamma^2 D_0 (\mathbf{G} + \langle \mathbf{G}_0 \rangle)^2 \tau_c^2 \right]^{-1}, \quad (19)$$

for the restricted diffusion regime. Here, $t_{G_{tot}}$ is the dephasing time associated to the magnetization $M(t_d) = \exp\left\{-\frac{1}{2}\beta(t_d)(\mathbf{G} + \langle \mathbf{G}_0 \rangle)^2\right\}$ decay to $1/e$, of the spin-bearing particles diffusing in a gradient $\mathbf{G}_{tot} = \mathbf{G} + \langle \mathbf{G}_0 \rangle$ in the respective diffusion regimes. Beyond these times, the higher order IGDT terms become more relevant.

The previous consideration are general for a cumulant expansion. In the following, we consider control strategies to enhance the IGDT terms contribution to the signal decay, while minimizing the loss of signal due to the pure interaction with the applied gradient. We need to enhance the terms that include the cross-overlap matrix $\beta^{0G}(t)$ in the IGDT expansion of Eq. (15). We thus look for conditions on the overlap matrices $\beta^{GG}(t_d)$ and $\beta^{0G}(t_d)$ that increase the *cross-terms* contribution with respect to the *pure applied* one.

We find that requesting the matrix difference $|\beta^{0G}(t_d)| - \beta^{GG}(t_d)$ to be positive-definite, enhance the IGDT terms contributions. Here, we define the modulus matrix $|\beta|$ as the matrix whose eigenvalues are the modulus of the eigenvalues of β . As the principal directions of all considered overlap matrices are defined by the ones of the correlation-time tensor τ_c , the positive-definite condition for $|\beta^{0G}(t_d)| - \beta^{GG}(t_d)$ is

$$|\beta_i^{0G}(t_d)| > \beta_i^{GG}(t_d) \quad i = 1, 2, 3, \quad (20)$$

where $\beta_i^{0G}(t_d)$ and $\beta_i^{GG}(t_d)$ are the eigenvalues of the corresponding overlap matrices. A derivation for this condition to enhance the IGDT contributions is found in the Appendix A. Notice that from Eq. (15), if the vector $\beta^{0G}(t_d) \langle \mathbf{G}_0 \rangle$ is orthogonal to the applied gradient, the second term vanishes independently on the relation (20). Then, the expression of Eq. (20) is a necessary but not sufficient condition.

The pure background gradient contribution is enhanced by minimizing the number of RF pulses, as its corresponding filter function lower the frequency of its dominant peak, thus maximizing the overlap with the displacement spectral density $\mathcal{S}(\omega)$ which is centered at zero frequency. The *cross-term* contributions are enhanced by increasing the applied gradient strength [see Eq. (15)], however this also enhance the pure applied gradient term. In order to avoid the latter effect, we increase the modulation frequency of the applied gradient to reduce the overlap of the applied gradient

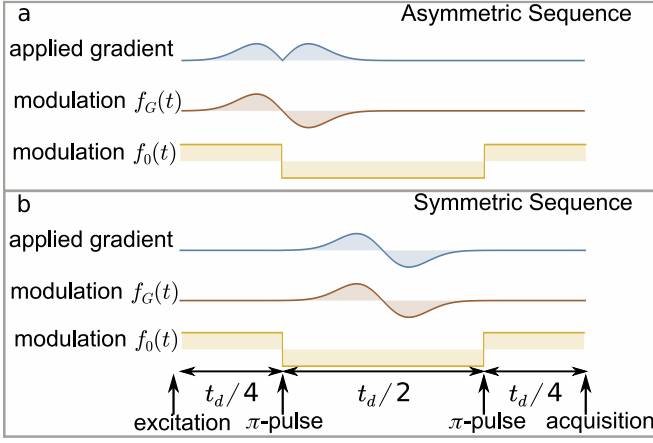


FIG. 5. Suitable design of *Symmetric* and *Asymmetric Sequences* of modulated gradients to probe the IGDTs. The sequences involve an initial excitation pulse followed by an applied gradient modulation defined by $f_G(t)$ given by Eq. (26). Together with two RF π -pulses at times $t = 1/4 t_d$ and $t = 3/4 t_d$ to modulate the background gradient as $f_0(t)$, determines the Gaussian derivative gradient spin-echo (GDGSE) sequence. This diffusion weighting block is then followed by an acquisition block. (a) *Asymmetric Sequence* and (b) *Symmetric Sequence*. In both sequences, the internal gradient modulation $f_0(t)$ corresponds to the one determined by the two RF pulses conforming a CPMG sequence that refocuses the decoherence due to susceptibility-induced magnetic field inhomogeneities. The applied gradient modulation is proportional to the first derivative of the Gaussian function as shown in Eq. (26). The spin dephasing due to interaction with the positive part of the applied gradient modulation is then refocused by the interaction with the negative part of the modulation. The modulation profile $f_G(t)$ in the *Asymmetric Sequence* is obtained by applying the gradient profile shown with the blue line in panel (b), as the RF π -pulses effectively change the sign of the phase evolution of the spins. The time interval in which the modulation $f_G(t)$ is significantly different from zero is lower than $1/2 t_d$.

filter function with the spectral density, thus reducing its dephasing effects. This can be done by concentrating the temporal variations of $f_G(t)$ in a small interval as can be seen in Fig. 5.

If the modulation frequency of the applied gradient becomes larger than the one of the background gradient modulation, the cross-filter overlap $\Re [F_0(\omega, TE) F_G^*(\omega, TE)]$ in Eq. (9) also is reduced. With the aim of increasing *the cross-terms* dephasing effect, we thus reduce the total duration of the applied gradient modulation to broaden its high-frequency peak and allow the overlap with the background gradient filter component at lower frequencies. This cross-filter overlap can be further maximized by synchronizing properly the sign changes of the applied and background gradient modulations to make a constructive interference between them as described in details in the Appendix B.

In order to attain the condition of Eq. (20), we reduce the effective interaction time of the spins with

the applied gradient, compared to the times they interact with the cross interference of the applied and background gradients. The effective interaction time of the background and applied gradients are the diffusion times during which the spins interact with each of these gradients,

$$T_0 = \int_0^{t_d} dt f_0^2(t) \quad (21)$$

and

$$T_G = \int_0^{t_d} dt f_G^2(t), \quad (22)$$

respectively. Similarly, the effective interaction time of *the cross-term* is the diffusion time that generates the cross interference between the applied and background gradients,

$$T_{0G} = \int_0^{t_d} dt f_0(t) f_G(t). \quad (23)$$

Therefore, to achieve the condition (20), we need $T_{0G} > T_G$. This latter condition can be seen more directly at the restricted diffusion limit, where we can approximate the overlap matrices as

$$\begin{aligned} \beta_{rest}^{GG}(t_d) &\approx \mathbf{S}(0) \gamma^2 \int_{-\infty}^{\infty} \frac{d\omega}{2\pi} |F_G(\omega, t_d)|^2 \\ &\approx \mathbf{S}(0) \gamma^2 \int_0^{t_d} dt f_G^2(t) \\ &\approx \mathbf{S}(0) \gamma^2 T_G \end{aligned} \quad (24)$$

and

$$\begin{aligned} \beta_{rest}^{0G}(t_d) &\approx \mathbf{S}(0) \gamma^2 \int_{-\infty}^{\infty} \frac{d\omega}{2\pi} \Re [F_0(\omega, t_d) F_G^*(\omega, t_d)] \\ &\approx \mathbf{S}(0) \gamma^2 \int_0^{t_d} dt f_0(t) f_G(t) \\ &\approx \mathbf{S}(0) \gamma^2 T_{0G}, \end{aligned} \quad (25)$$

being both proportional to the corresponding effective interaction times, as the displacement spectral density can be factored out from the overlap integral. A general demonstration is found in the Appendix A.

Applied gradients can be arbitrary modulated in general. However, the background gradient is only modulated by applying the RF π -pulses that invert the spin phase evolution, which is encoded in the modulation function $f_0(t)$ that switches between $+1$ and -1 at every time a π -pulses is applied. To enhance *the cross-term* effect with respect to *the pure applied term*, we thus propose the implementation of smooth modulations for the applied gradient that satisfy the condition $|f_G(t)|^2 < |f_0(t)|$, and a synchronization of the sign changes of $f_0(t)$ and $f_G(t)$ such that $f_0(t) f_G(t) = |f_G(t)|$ (Fig. 5).

To get a MGSE sequence, the applied gradient modulation $f_G(t)$ must cross zero at least once. The condition $f_0(t)f_G(t) = |f_G(t)|$ can be attained by setting a smooth MGSE with an applied gradient modulation with a single refocusing echo, whose zero crossing time matches the instant of time where the RF π -pulse is applied to modulate the background gradient function $f_0(t)$. To avoid further sign inversions in $f_0(t)f_G(t)$, the applied gradient modulation $f_G(t)$ must vanish every time that a π -pulse is applied. Figure 5a shows an example of such a modulation. Thus, all of these conditions define a general *asymmetric sequence* that enhance the IGDT *cross-term* contributions.

To probe directly the IGDT terms proportional to $\beta^{GG}(t_d)$ and $\beta^{00}(t_d)$, we must cancel *the cross-term* dephasing effect in Eq. (15), while keeping invariant *the pure terms*. We thus make $\beta^{0G}(t_d) = 0$ by setting $f_G(t)$ an odd function with respect to its middle time and $f_0(t)$ an even function again with respect to its middle time. Then, the cross-filter vanishes by matching the modulation centers of $f_G(t)$ and $f_0(t)$. Figure 5b shows an example of such modulation sequence. The pure overlap matrices $\beta^{GG}(t_d)$ and $\beta^{00}(t_d)$ thus remain invariant, because temporal shifts of the corresponding modulation functions does not alter the squared modulus of their Fourier transform. This shifted modulation thus define a general *symmetric sequence*.

Finally, to maximize the background gradient dephasing effects with the overlap integrals $\beta^{00}(t_d)$ and $|\beta^{0G}(t_d)|$, we have to modulate the background gradient with a low frequency to maximize their overlap with the displacement spectral density $\mathcal{S}(\omega)$. We thus need a modulation sequence with the minimal possible number of pulses. As we require that $f_0(t)$ be an even function, we choose a Carr-Purcell-Meiboom-Gill (CPMG) sequence [71, 72] with two pulses for its modulation. The RF π -pulses are thus applied at $t = 1/4t_d$ and $t = 3/4t_d$ respectively (Fig. 5).

In the Appendix A, we show that the relation of Eq. (20) is fulfilled assuming the sequence conditions derived in this section for an arbitrary diffusion regime.

In summary, to enhance *the cross-term* effects, the background gradient modulation $f_0(t)$ has to be an even function with respect to $t_d/2$ with a minimal number of pulses. The applied gradient modulation has to be an MGSE sequence with a smooth modulation function such that $|f_G(t)| \leq 1$, with a single refocusing echo matching the zero crossing time with a π -pulse that modulate $f_0(t)$. The modulation function $f_G(t)$ has to be an odd function with respect to its middle time, *i.e.* the zero crossing time, and should vanish also at every π -pulse that modulate $f_0(t)$.

4.3. Paradigmatic example: Gaussian derivative modulation

To follow the above sequence design, we propose here a paradigmatic MGSE sequence with applied gradient modulations derived from a Gaussian function derivative. We call it the Gaussian derivative gradient spin-echo (GDGSE) modulation that allow us to obtain analytical calculations. The GDGSE sequence consists on a modulation function $f_G(t)$ determined by the first derivative of a Gaussian function centered at $t_d/2$ with a standard deviation given by a fraction αt_d of the total diffusion time t_d (see Fig. 5b)

$$f_G(t) = \frac{\sqrt{e}}{\alpha t_d} (t - t_d/2) e^{-\frac{(t-t_d/2)^2}{2\alpha^2 t_d^2}}. \quad (26)$$

Here, $\alpha \ll 1$ is a coefficient that controls the Gaussian modulation width.

The modulation function is normalized such that it satisfies $\max[f_G(t)] = 1$, so as the maximum gradient strength G is achieved. While the GDGSE allows us to obtain analytical expressions for the dephasing, its modulation is not finite along the time domain. As the applied gradient modulation decays exponentially for times $t \gg \alpha t_d$, we set the parameter $\alpha \ll 1$ to make negligible its modulation amplitude at every RF π -pulse and outside the considered diffusion time interval t_d . We thus consider negligible the modulation amplitude at the RF pulses $f_G(1/4t_d) = f_G(3/4t_d) \approx 0$ and outside the diffusion probing time. For example, by setting $\alpha = 1/15$, the modulation amplitude at the RF pulses and outside the probing time is $\lesssim 10^{-3}$. This requirement for α also provides a large frequency for the applied gradient modulation as required in Sec. 4.2 and, at the same time, reduces the effective interaction time of the applied gradient of Eq. (22).

The *asymmetric sequence* is obtained by shifting the modulation function $f_G(t)$ by $t_d/4$ to the left, as seen in Fig. 5a. To ensure a significant integral overlap between the applied and background gradient filters $\Re[F_0(\omega, t_d)F_G^*(\omega, t_d)]$, the coefficient α must not be too small. We found that $1/30 \lesssim \alpha \lesssim 1/10$ works well enough. To find a proper α , we need to compare the GDGSE filter maximum $|F_G(1/(\alpha t_d), t_d)|^2$ [see Eq. (C3) in Appendix C] with the GDGSE filter value at the modulation frequency of the background gradient $2\pi/t_d$. For $\alpha = 1/15$, for example, $|F_G(2\pi/t_d, t_d)|^2 / |F_G(1/(\alpha t_d), t_d)|^2 = 0.4$.

4.4. Overlap matrix weightings for diffusion asymptotic limits

Here we consider two physically relevant asymptotic regimes to evaluate the overlap matrix weighting on the IGDT expansion terms, the free diffusion ($t_d/\tau_c \ll 1$) and the restricted diffusion ($t_d/\tau_c \gg 1$) limits. The

general expressions for the overlap integrals of Eqs. (7-9), can be found in the Appendix C. As expected at the free diffusion regime, the behavior of the three overlap functions is cubic on the evolution time. If the condition $t_d/\tau_c \ll 1$ is fulfilled in all spatial directions, the diffusion can be assumed isotropic. The overlap integrals are then scalars as all principal directions are equivalent, where

$$\beta_{free}^{GG}(t_d) = 2e\sqrt{\pi}\gamma^2 D_0 \alpha^3 t_d^3 \quad (27)$$

and

$$\beta_{free}^{00}(t_d) = \frac{\gamma^2 D_0}{24} t_d^3. \quad (28)$$

As we consider $\alpha \ll 1$ to make $f_G(t + t_d/4) \approx 0$ at the edge of the interval $[0, t_d/2]$, the free diffusion limit of the cross overlap function gives the cross overlap

$$\beta_{free}^{0G}(t_d) = \sqrt{\frac{\pi e}{2}} \left(1/\alpha - 4\sqrt{\frac{2}{\pi}} \right) \gamma^2 D_0 \alpha^3 t_d^3. \quad (29)$$

Instead, at the restricted diffusion limit, all the overlap matrices are lineal as a function of the diffusion time

$$\beta_{rest}^{GG}(t_d) = e\sqrt{\pi}\gamma^2 D_0 \tau_c^2 \alpha t_d, \quad (30)$$

$$\beta_{rest}^{00}(t_d) = 2\gamma^2 D_0 \tau_c^2 (t_d - 5\tau_c). \quad (31)$$

Again, as $\alpha \ll 1$, the restricted diffusion limit of the cross overlap matrix can be approximated as

$$\beta_{rest}^{0G}(t_d) = 4\sqrt{e}\gamma^2 D_0 \tau_c^2 \alpha t_d. \quad (32)$$

The advantage of using the smooth gradient modulations to obtain the positive-definite condition for the matrix $|\beta^{0G}(t_d)| - \beta^{GG}(t_d)$ compared with sharp ones that switch the gradient sign between $\{-1, +1\}$, can be seen in these asymptotic behaviors. The ratios between the overlap matrices for $\alpha \ll 1$ are $\beta_{free}^{0G}(t_d)/\beta_{free}^{GG}(t_d) = \sqrt{\frac{e}{2}} \left(1/\alpha - 4\sqrt{\frac{2}{\pi}} \right) / (2e) > 1$ in the free diffusion limit and $\beta_{rest}^{0G}(t_d)/\beta_{rest}^{GG}(t_d) = 4\sqrt{e}/(e\sqrt{\pi}) > 1$ in the restricted one. On the other hand, a sharp modulation that only switches the gradient sign between $\{-1, +1\}$, can attain, at the most, the same effective interaction times for the spin interaction with the applied gradient and with the cross-interference between the applied and background gradients. Then, it is not possible to minimize the interaction effects with the applied gradient without also reducing the cross-interaction effects in the same ratio, and thus no enhancement of the cross IGDT terms is found.

5. THE IGDT EXPANSION IN TYPICAL BRAIN TISSUE CONDITIONS

In this section we evaluate the IGDT expansion assuming typical values of the free diffusion coefficient

and correlation times in brain tissues. The diffusion coefficient typically belongs to the range starting from $0.8 \mu\text{m}^2/\text{ms}$ to $2.2 \mu\text{m}^2/\text{ms}$ for human brain [94–96] and $3 \mu\text{m}^2/\text{ms}$ for free water at 37°C [97]. Brain tissue microstructure sizes range for example for the axon radius, typically between the interval $0.3 \mu\text{m}$ – $3 \mu\text{m}$ in human brain [18, 98, 99]. Assuming cylindrical geometries with a restriction radius between this range, the expected diffusion correlation time τ_c ranges from 10^{-2} ms to 10 ms, based on the Fick-Einstein equation $l_c^2 = D_0 \tau_c$.

The internal magnetic field variations are of order of $10^{-6} B_0$ [24, 29, 62]. Intra and extra-axonal internal gradients in white matter show mono-disperse internal gradient distribution centered at zero and with a distribution width that is maximum in a direction perpendicular to the axon direction [24, 29, 30, 62]. This was also demonstrated with capillary tube phantoms mimicking the axon morphology giving internal gradient width of the order of 1 mT/m on a 1 T magnet [24]. Numerical calculations of internal gradients in axon bundles using the AxonPacking open-source software [100] and a Finite Perturber Method (FPM) [24, 101], predict internal gradient widths on the range of 20-200 mT/m in a 9.4T magnet [63]. As internal gradients scale with the tissue compartmentalization characteristic length l_c , internal gradient variations can be estimated by $\Delta G_0 \approx 10^{-6} B_0 / l_c$. Then, $\Delta G_0 \approx 1000$ mT/m can be expected in brain tissues, consistently with observations in numerical simulations [63]. However, the highest internal gradient strengths are typically concentrated only in small spatial regions, so that the molecular movement averages them, reducing their values effectively, thus making the standard deviation of internal gradient distribution smaller.

To evaluate the main features of the IGDT-expansion, we focus on a 1-dimensional analysis associated with the diffusion process in one of the principal axis of the correlation time tensor τ_c . The analysis is equivalent for the three principal axes, in which the only relevant aspect is how it scales with the corresponding τ_c . According to Eq. (15), the IGDT-expansion then reduces to

$$\begin{aligned} \ln M(t_d) = & -\frac{1}{2} G^2 \beta_{GG}(t_d) - G \beta_{0G}(t_d) \langle G_0 \rangle \\ & - \frac{1}{2} \beta_{00}(t_d) \langle G_0^2 \rangle \\ & + \frac{1}{2} G^2 \beta_{0G}^2(t_d) \langle \Delta G_0^2 \rangle \\ & + G \beta_{0G}(t_d) \beta_{00}(t_d) \langle G_0 \rangle \langle \Delta G_0^2 \rangle \\ & + \frac{1}{2} \beta_{00}^2(t_d) \langle G_0 \rangle^2 \langle \Delta G_0^2 \rangle + \mathcal{O}[\langle \Delta G_0^3 \rangle]. \end{aligned} \quad (33)$$

To model the diffusion process, we consider an OU process in one spatial dimension and the gradient ensemble description of Sec. 2.2. The IGDT-expansion better approximates the real signal if the applied gradient

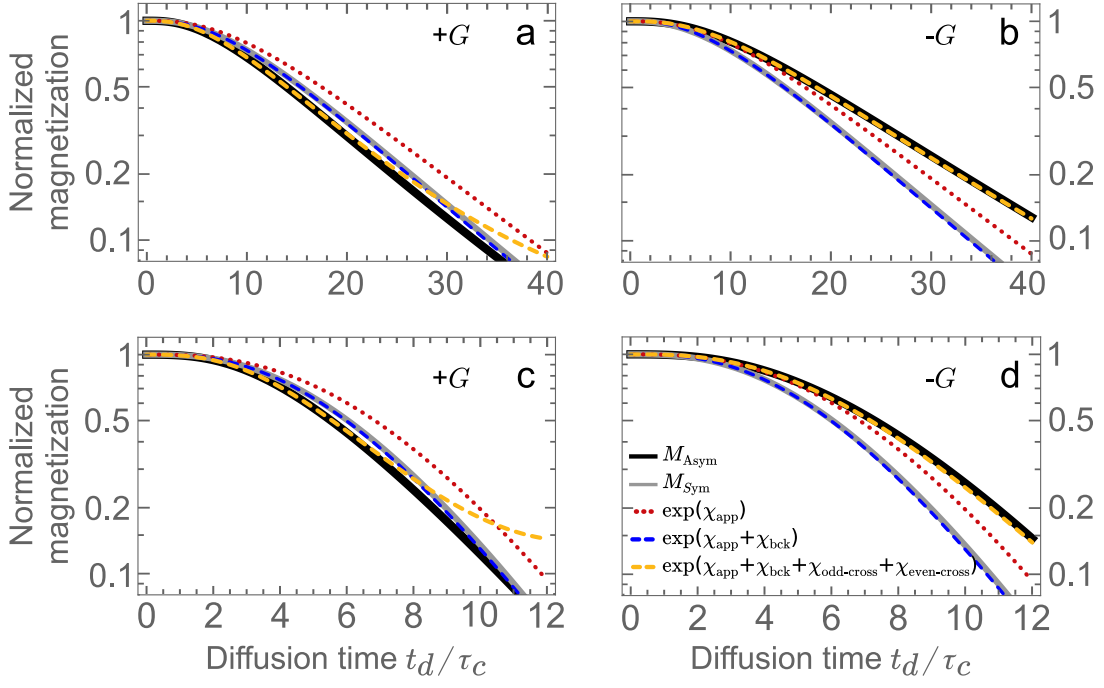


FIG. 6. Contribution of different terms of the IGDT expansion. The solid black lines correspond to the magnetization signal produced by the *asymmetric sequence*, while the gray ones corresponds to the signal produced by the *symmetric sequence*. These signals are calculated numerically by averaging the magnetization signal with a Gaussian distribution for the background gradient G_0 with a standard deviation $\Delta G_0 = 0.15|G|$, and mean value $\langle G_0 \rangle = 0.1|G|$ in panels (a, c) and with opposite sign in panels (b, d). The red dotted line corresponds to *the pure applied gradient* contribution ($\chi_{\text{app}} = \chi_{G^2}$), the blue dashed line includes also *the pure background gradient* contribution ($\chi_{\text{bck}} = \chi_{0^2} + \chi_{0^2\Delta^2}$). The yellow dashed lines includes *the cross-terms* contributions $\chi_{\text{odd-cross}} = \chi_{0G} + \chi_{0G\Delta^2}$ and $\chi_{\text{even-cross}} = \chi_{G^2\Delta^2}$. We consider the free diffusion coefficient $D_0 = 2.2 \mu\text{m}^2/\text{ms}$, a correlation time $\tau_c = 2 \text{ ms}$ in panels (a, b) and $\tau_c = 5 \text{ ms}$ in panels (c, d) corresponding to restriction lengths of $2 \mu\text{m}$ and $3.3 \mu\text{m}$, and a giromagnetic factor of $\gamma = 267 \text{ mT}^{-1}\text{ms}^{-1}$. In panel (a) and (b) the applied gradient is $G = 600 \text{ mT/m}$ and in panels (c) and (d) $G = 400 \text{ mT/m}$.

is stronger than the standard deviation of internal gradient distribution $G \gg \Delta G_0$. Here we assume a Gaussian distribution for the internal gradients with mean $\langle G_0 \rangle = 0.1G$ and standard deviation $\Delta G_0 = 0.15G$ for the internal gradients. Based on the reported values of internal magnetic field variations in brain tissue [29], we consider for our simulations two cases for the relation between the applied and internal gradients $G = 600 \text{ mT/m}$, $\langle G_0 \rangle = 60 \text{ mT/m}$ and $G = 400 \text{ mT/m}$, and $\langle G_0 \rangle = 40 \text{ mT/m}$. The internal gradient distribution widths are thus $\Delta G_0 = 90 \text{ mT/m}$ and $\Delta G_0 = 60 \text{ mT/m}$, respectively.

Based on Eq. (4), we first calculate the magnetization average of the spin-bearing particles diffusing in presence of a given internal gradient strength G_0 . The thermal diffusion follows the OU Gaussian process as described in Sec. 3.2 for the spin's random phase. The resulting magnetization average thus only depends on the second cumulant of the spin phase

$$M(t_d, G_0) = e^{-\frac{1}{2}\langle\langle\phi(t_d, G_0)^2\rangle\rangle}, \quad (34)$$

with $\langle\langle\phi(t_d, G_0)^2\rangle\rangle = G^2\beta_{GG}(t_d) + 2G_0G\beta_{0G}(t_d) + G_0^2\beta_{00}(t_d)$. Notice that this second cumulant is equal to the one in Eq. (6) for a given G_0 value, *i.e.* without

yet considering the internal gradient distribution. The overlap functions $\beta_{GG}(t_d)$, $\beta_{00}(t_d)$ and $\beta_{0G}(t_d)$ are given by the eigenvalues corresponding to the considered principal axes of the attenuation matrices of Eqs. (7-9). Then, we calculate the total magnetization decay by averaging Eq. (34) over the internal gradient distribution.

The magnetization signal for the *asymmetric sequence* described in Fig. 5a includes the *cross-term* in the gradient average

$$M_{\text{Asym}}(t_d) = e^{-\frac{1}{2}G^2\beta_{GG}(t_d)} \times \left\langle e^{-G_0G\beta_{0G}(t_d)} e^{-\frac{1}{2}G_0^2\beta_{00}(t_d)} \right\rangle. \quad (35)$$

Instead, the cross overlap integral $\beta_{0G}(t_d)$ vanishes for the *symmetric sequence* described in Fig. 5b, and thus the magnetization signal is

$$M_{\text{Sym}}(t_d) = e^{-\frac{1}{2}G^2\beta_{GG}(t_d)} \left\langle e^{-\frac{1}{2}G_0^2\beta_{00}(t_d)} \right\rangle. \quad (36)$$

Typical relaxation times T_2 of white and gray matter in brain tissue are on the order of $\sim 50 - 130 \text{ ms}$ [102–104]. We thus evaluate the effects of the different groups

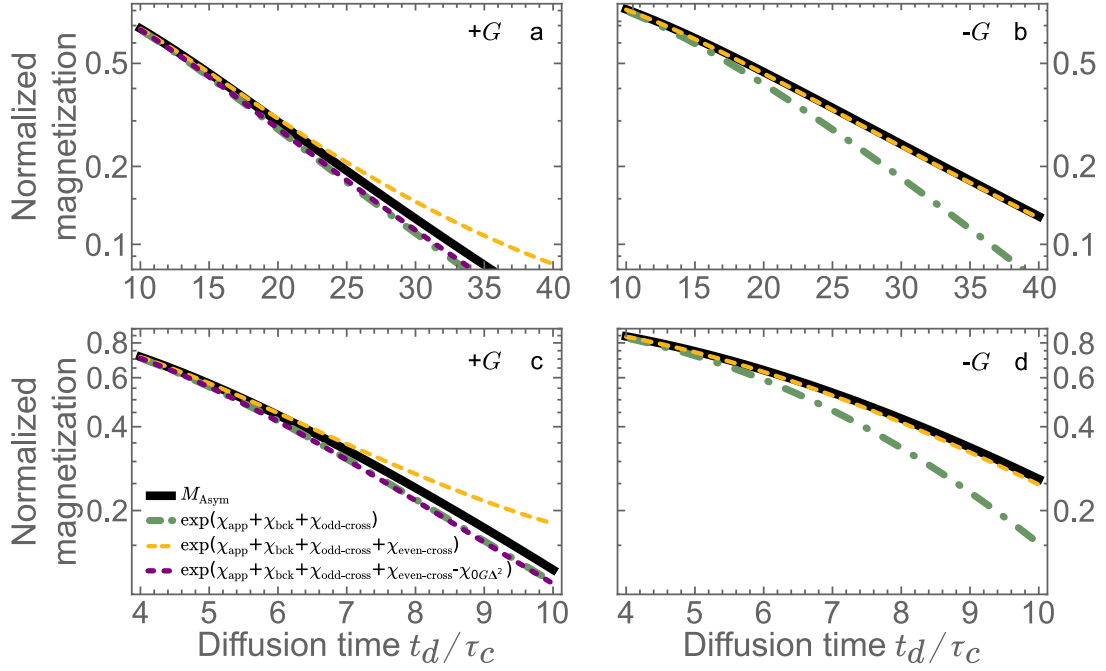


FIG. 7. Contribution of different terms of the IGDT expansion to the magnetization signal produced by the *asymmetric sequence* (solid black lines). The green dot-dashed lines include the *pure applied* ($\chi_{\text{app}} = \chi_{G^2}$), *pure background* ($\chi_{\text{bck}} = \chi_{0^2} + \chi_{0^2\Delta^2}$) and *odd cross-terms* contribution ($\chi_{\text{odd-cross}} = \chi_{0G} + \chi_{0G\Delta^2}$). The yellow dashed lines includes also the *even cross-term* contribution $\chi_{\text{even-cross}} = \chi_{G^2\Delta^2}$. The purple dashed line consider all the terms in the yellow curve subtracting the *odd-cross term* $\chi_{0G\Delta^2} = G\beta_{0G}(t_d)\beta_{00}(t_d)\langle G_0 \rangle \langle \Delta G_0^2 \rangle$. As in Fig. 6, we consider the free diffusion coefficient $D_0 = 2.2 \mu\text{m}^2/\text{ms}$, a correlation time $\tau_c = 2 \text{ ms}$ in panels (a, b) and $\tau_c = 5 \text{ ms}$ in panels (c, d), and a giromagnetic factor $\gamma = 267 \text{ mT}^{-1}\text{ms}^{-1}$. In panel (a) and (b) the applied gradient is $G = 600 \text{ mT/m}$ and in panels (c) and (d) $G = 400 \text{ mT/m}$.

of terms in the IGDT-expansion before this time scale to be able to predict the reliability to measure them. Figure 6 shows two relevant experimental situations, a restricted (Figs. 6a,b) and a free diffusion (Figs. 6c,d) regime. For illustration, we assumed the free diffusion coefficient $D_0 = 2.2 \mu\text{m}^2/\text{ms}$ in Fig. 6. It is still unknown the free diffusion coefficient in brain tissue, as typically only the apparent diffusion coefficient is measured. If the free diffusion coefficient is lower than the assumed one, the magnetization decay becomes slower and thus more diffusion time is required for probing the IGDT effects. For example, if the free diffusion coefficient reduces to $D_0 \approx 0.7 \mu\text{m}^2/\text{ms}$, the behavior of the curves of Fig. 6 would decay to 10% of the initial magnetization at 100 ms instead of 40 ms in the cases of panels a and b; and at 20 ms instead of 12 ms in the cases of panels c and d. Diffusion times that allow probing the IGDT effects are thus still accessible for the typical T_2 values of white and gray matter in brain even in this scenario.

We consider applied gradient modulations with opposite gradient directions to show the behavior of the *odd* and *even cross terms* in the cumulant expansion. In both regimes, the magnetization of the *symmetric sequence* is well described by the *pure applied* $\chi_{\text{app}} = -\frac{1}{2}G_i\beta_{ij}^{GG}(t_d)G_j$ and *pure background gradient terms* $\chi_{\text{bck}} = \chi_{0^2} + \chi_{0^2\Delta^2} + \chi_{0\Delta^3}$ of the IGDT-expansion of Eq. (33) (see table I). Notice that the *pure background*

gradient terms increase the magnetization decay with respect to the decay produced by only considering a *pure applied gradient term*. This is a consequence of the fact that the *total background gradient term* is negative as the first term $\chi_{0^2} = -\frac{1}{2}\beta_{00}(t_d)\langle G_0^2 \rangle$ is larger than the next term $\chi_{0^2\Delta^2} = \frac{1}{2}\beta_{00}^2(t_d)\langle G_0 \rangle^2 \langle \Delta G_0^2 \rangle$ with opposite sign. As we discussed in Sec. 3.3, the lower order terms in the cumulant expansion with lower power law exponents of overlap matrices are dominant at short times $t_d < t_{G_{\text{tot}}}$, where $t_{G_{\text{tot}}}$ is given by Eqs. (18) and (19), depending on the diffusion regime. At longer times $t_d > t_{G_{\text{tot}}}$, the higher order terms become relevant and they might then reduce the overall decay. By reducing the effective interaction time of the applied gradient with respect to the one of the background gradient, as done in the sequence of Fig. 5, also makes the *pure background gradient terms* more significant with respect to the pure applied terms.

Then, by including the *cross-terms* $\chi_{\text{odd-cross}} + \chi_{\text{even-cross}} = \chi_{0G} + \chi_{0G\Delta^2} + \chi_{G^2\Delta^2}$ of the expansion (33) (see Table I), we reproduce the magnetization decay generated by the *asymmetric sequence* (Figs. 6b,d). In Figs. 6b,d there is a better convergence than in Figs. 6a,c, where the convergence is poor for $t_d > 25\tau_c$ and $t_d > 7\tau_c$, respectively. The performance difference of the cumulant expansion is due to the relative direction between the applied and average background gradient

that change the sign of *the odd cross-terms*.

We now analyze this effect on the signal decay. The first two *odd cross-terms* $\chi_{0G} = -G\beta_{0G}(t_d)\langle G_0 \rangle$ and $\chi_{0G\Delta^2} = G\beta_{0G}(t_d)\beta_{00}(t_d)\langle G_0 \rangle \langle \Delta G_0^2 \rangle$ that we consider here, have opposite signs. Then, the behavior of their overall decay contribution at short times is the opposite of the one at longer times. *The even cross-term* $\chi_{G^2\Delta^2} = \frac{1}{2}G^2\beta_{0G}^2(t_d)\langle \Delta G_0^2 \rangle$ is always positive and it thus always reduce the magnetization decay. As it contains a quadratic order on the attenuation overlap function, $\beta_{0G}^2(t_d)$ becomes relevant at long times $t_d > t_{G_{tot}}$ (see Eqs. 18 and 19). This is seen at times longer than $\sim 15\tau_c$ in Fig. 7b, and at times longer than $\sim 6\tau$ in Fig. 7d, when the green dash-dotted curve starts to deviate from the exact decay (black line), and the dashed yellow line continues reproducing the expected behavior.

In Fig. 6a and 6c, the applied gradient has the same sign as the background gradient $\langle G_0 \rangle$. *The pure background gradient term* χ_{0^2} and *the odd cross-term* χ_{0G} thus contribute by increasing the magnetization decay at short times, as both terms are negative. At longer times the behavior changes, as *the odd cross-term* $\chi_{0G\Delta^2}$ and *the even cross-term* $\chi_{G^2\Delta^2}$ now tend to reduce the magnetization decay because they are positive. In these cases, the dashed yellow line diverges from the expected signal behavior at times longer than $25\tau_c$ in Fig. 7a and at times longer than $7\tau_c$ in Fig. 7c. At these times the terms $\chi_{0G\Delta^2}$ and $\chi_{G^2\Delta^2}$ become more relevant. This shows the slow convergence of the IGDT expansion when the applied gradient is in the same direction of the mean background gradient. In this case, we obtain a better approximation by including only *the even cross-term* $\chi_{G^2\Delta^2}$ such as

$$\ln M(t_d) = \chi_{app} + \chi_{bck} + \chi_{0G} + \chi_{G^2\Delta^2},$$

and excluding the *odd cross-term* $\chi_{0G\Delta^2}$ or *vice versa*

$$\ln M(t_d) = \chi_{app} + \chi_{bck} + \chi_{0G} + \chi_{0G\Delta^2}.$$

Figures 7a and c show that these expansion's approximations (purple dashed line and green dot-dashed respectively) reproduce better the predicted curve (black line).

In Fig. 6b and 6d, the applied gradient has the opposite sign of the average background gradient $\langle G_0 \rangle$. In this case, the signal decay is reduced at short times since the leading *odd cross-term* χ_{0G} reduces the magnetization decay. At long times $t_d > t_{G_{tot}}$ (see Eqs. 18 and 19), *the even cross-term* $\chi_{G^2\Delta^2}$ and the *odd cross-term* $\chi_{0G\Delta^2}$ have opposite behavior allowing a better convergence (Fig. 7b and d). As a result, the contrast ratio $M_{Asym}(t_d)/M_{Sym}(t_d)$ between the magnetization of the *asymmetric* and *symmetric sequences* is maximized when applied and background gradient are in the opposite direction compared with the case when they are in the same direction.

As shown in Fig. 7a and c, when the applied gradient has the same direction as the background gradient, the

green and purple curves are good approximation and indistinguishable between them. In the green curve, we exclude *the even-cross term* $\chi_{G^2\Delta^2}$ and in the purple curve, *the odd-cross term* $\chi_{0G\Delta^2}$ from the expansion. As it is arbitrary which of them is excluded, we propose under this condition to approximate *the even-cross term* from

$$\begin{aligned} 1/2\chi_{even-cross} \approx & 1/2 \ln M_{Asym,+G} + 1/2 \ln M_{Asym,-G} \\ & - \ln M_{Sym}, \end{aligned} \quad (37)$$

rather than from Eq. (17) by excluding the term $\chi_{even-cross}$ from $\ln M_{Asym,+G}$. To determine *the odd*

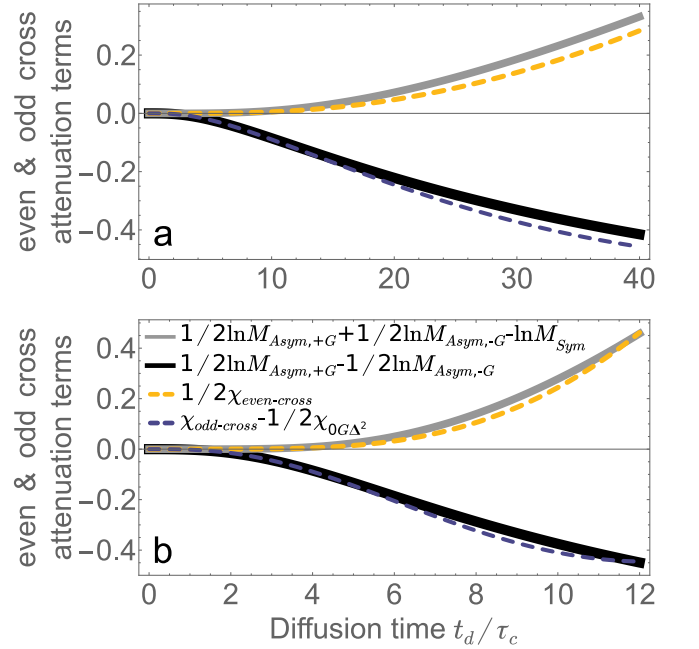


FIG. 8. Approximated *even* and *odd cross-term* attenuations when the applied gradient has the same direction as the background gradient. The gray and black solid lines gives the approximated *even* and *the odd cross-terms* following Eqs. (37) and (38) respectively, calculated from the mathematical operations between the magnetization signal of the *symmetric* and *asymmetric sequences* with the two applied gradient directions. These magnetization signals are calculated numerically by averaging the magnetization signal with a Gaussian distribution for the background gradient G_0 with a standard deviation $\Delta G_0 = 0.15|G|$, and mean value $\langle G_0 \rangle = 0.1|G|$. The yellow and purple dashed lines show the corresponding *even cross-term* $1/2\chi_{even-cross} = 1/2\chi_{G^2\Delta^2}$ and *the odd cross-term* $\chi_{0G} + 1/2\chi_{0G\Delta^2} = \chi_{odd-cross} - 1/2\chi_{0G\Delta^2}$ of the left-hand-side of Eqs. (37) and (38) respectively, derived from the expansion of Eq. (33). As in Fig. 6, we consider the free diffusion coefficient $D_0 = 2.2 \mu\text{m}^2/\text{ms}$, a correlation time $\tau_c = 2$ ms in panel (a) and $\tau_c = 5$ ms in panel (b), and a giromagnetic factor $\gamma = 267 \text{mT}^{-1}\text{ms}^{-1}$. In panel (a) the applied gradient is $G = 600 \text{mT/m}$ and in panel (b) $G = 400 \text{mT/m}$.

cross-term, then use the approximation

$$\begin{aligned} \chi_{0G} + 1/2\chi_{0G\Delta^2} &= \chi_{\text{odd-cross}} - 1/2\chi_{0G\Delta^2} \\ &\approx 1/2 \ln M_{\text{Asym},+\mathbf{G}} - 1/2 \ln M_{\text{Asym},-\mathbf{G}}, \end{aligned} \quad (38)$$

rather than Eq. (16) by excluding the term $\chi_{0G\Delta^2}$ from $\ln M_{\text{Asym},+\mathbf{G}}$. Figure 8 shows the validity of these assumptions.

6. VALIDITY OF THE INTERNAL GRADIENT ENSEMBLE MODEL

The internal gradient distribution that we estimate with the proposed method is an effective gradient distribution resulting from the motional averaging of the spin-bearing particles [22]. The internal gradient ensemble model implicitly simplifies the signal attenuation effects due to the spin movement in a space-dependent gradient field to the one induced by the spin movement in an effective constant internal gradient. Here, we thus evaluate the reliability of this assumption through the simulations of the magnetization decay of spin-bearing particles diffusing in a sinusoidal gradient field that models typical field inhomogeneities in porous systems [32, 63, 105].

For this evaluation, we perform simulations in one spacial dimension by setting an applied gradient G and an inhomogeneous background magnetic field with a z -component

$$\Delta B_0(x) = g \frac{\lambda}{2\pi} \cos\left(\frac{2\pi}{\lambda}x\right), \quad (39)$$

where g is the maximum internal gradient strength and λ is the wavelength of the inhomogeneous internal field fluctuation. We consider four scenarios in Fig. 9, free and restricted diffusion regimes, where the internal magnetic field inhomogeneity wavelength λ is larger than and comparable to the diffusion restriction length l_c . We do not consider the case when the wavelength λ is shorter than the diffusion restriction length l_c , as the signal decay depends only on a averaged internal gradient value.

For the simulations, we evaluated 5000 stochastic realizations of an OU process of mean spin position x_0 using a free diffusion coefficient $D_0 = 2 \mu\text{m}^2/\text{ms}$ and a diffusion correlation time $\tau_c = 10 \text{ ms}$. The initial spin position x_0 is set randomly within the spatial interval $(-\lambda, \lambda)$. We then calculate the spin magnetization signal of the diffusing spins in presence of the considered internal magnetic field inhomogeneity, together with a constant applied gradient with π -pulse at the diffusion time $t_d/2$ to provide a spin-echo modulation sequence.

The simulations are shown in Fig. 9, where the black dashed curves are the exact predicted signal. The blue dashed lines are the magnetization signal predicted by the internal gradient ensemble model. It is calculated using Eq. (35) and determined by the effective gradient distribution resulting from the motional averaging of the

gradient seen by the spin from the beginning of the sequence to the total diffusion time

$$G_0^i = \frac{1}{t_d} \int_0^{t_d} dt \frac{d}{dx} \Delta B_0(x_i(t)). \quad (40)$$

Here, the magnetic field shift $\Delta B_0(x)$ is given by Eq. (39), G_0^i is the effective internal gradient seen by the i th spin-bearing particle along the $x_i(t)$ position trajectory. With the effective internal gradients G_0^i , we then generate a histogram as shown in blue in the insets of Fig. 9 compared with the real gradient distribution in black. The red dotted curves correspond to the magnetization decay only due to the interaction with the applied gradient and the yellow solid lines correspond to the predicted signal derived from the IGDT expansion of Eq. (33). In the four considered cases the expected signals derived from the cumulant expansion and internal gradient ensemble model are in good agreement with the simulated, exact one. Thus, this result shows that the effects in the magnetization decay of spin-bearing particles, diffusing in internal gradients that depend on its position, can be reduced to an effective internal gradient distribution based on an ensemble of gradients. Moreover, the magnetization signal decay is shown to be characterized only by the moments of the effective internal gradient distribution.

The presented simulations thus show the relevance and good signal prediction of the developed model to describe the complex diffusion process in presence of magnetic field inhomogeneities induced by magnetic susceptibility heterogeneity in porous systems. Yet, we envisage some limitations. While the strength of the model is to reduce the complexity of the internal magnetic field heterogeneity to an internal gradient ensemble model characterized by the main moments of the distribution, it can only determine those moments and not the full internal gradient distribution. Thus, for example, the method is unable to provide information about multimodal gradient distributions. The molecular diffusion process can narrow the effective gradient distribution seen by the spins around its mean value as shown in Fig. 9d. Then, depending on the real gradient distribution variance, if the diffusion mean squared displacement is on the order of λ , the effective gradient variance may be much smaller than the real one or even the IGDT effects may vanish. While the predicted signal might be in agreement with the exact signal, as in Fig. 9d, some quantitative information about gradient field heterogeneities might be lost. However, while this still has to be demonstrated, this limitation is probably a physical limitation due to the motional averaging, and not due to the assumed model.

Another limitation is imposed by the time domain where the cumulant expansion is valid, defined by its convergence radius t_{conv} [75, 106]. The cumulant expansion of Eq. (5) is valid for times shorter than its convergence radius, defined by $t_{\text{conv}} = |z|$ with z being the complex solution of $M(z) = 0$ and $M(z)$ the

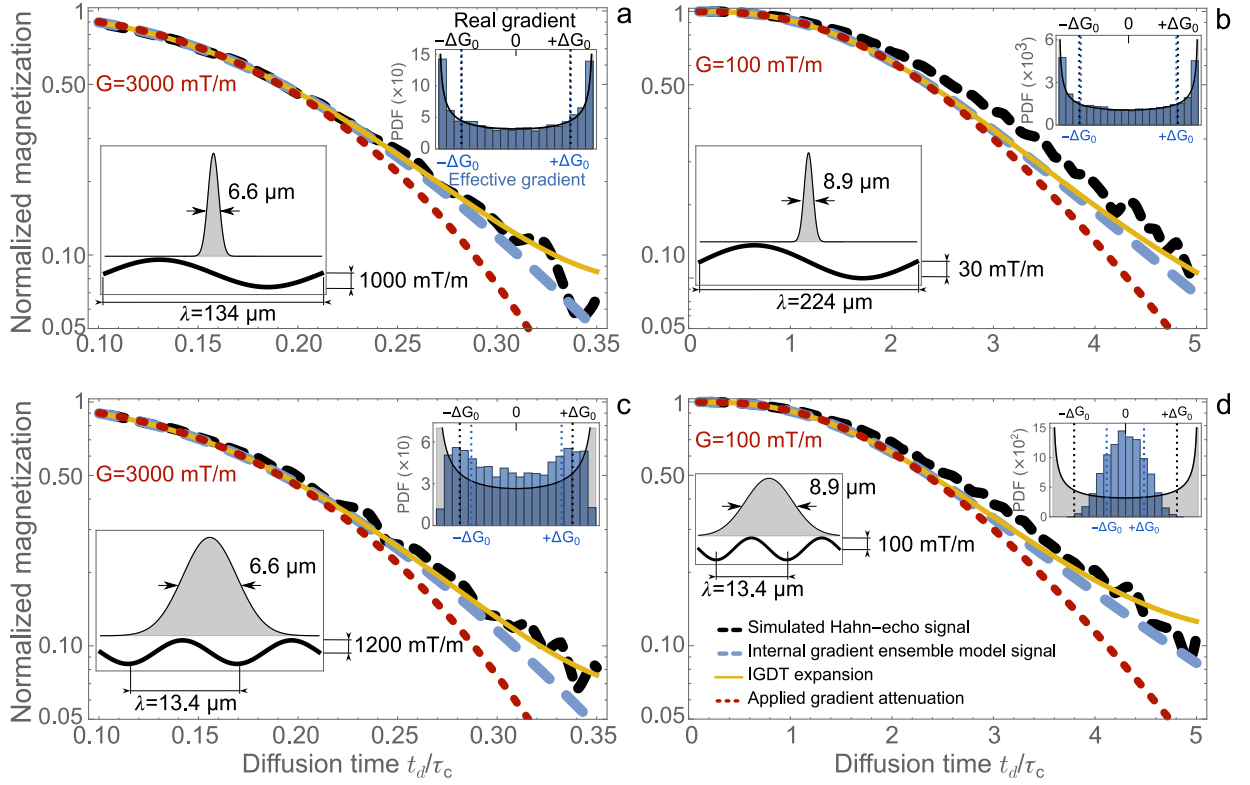


FIG. 9. Comparison of the predicted signal derived from the internal gradient ensemble model and the cumulant expansion framework with the exact signal of spin diffusion in an inhomogeneous magnetic field. Simulation of the magnetization decay of spin diffusion in an inhomogeneous magnetic field shown in the left inset of each panel in black solid line. The insets also show the relation between the background internal gradient wavelength and the diffusion length of the spin-bearing particles determined by the Gaussian distribution of the spin positions at the maximum diffusion times plotted in the main panels [$t_d = 3.5$ ms (a,c) and 50 ms (b,d)]. The insets on the right of each panel compare the real internal gradient distribution (black solid curve) with the effective one seen by the spins due to the motional averaging (blue histogram). Their corresponding standard deviations are shown with dashed vertical lines. The black dashed line in the main panels corresponds to the simulated magnetization for the considered spin-echo sequence of an ensemble of 5×10^3 spin-bearing particles driven by an OU process in presence of the sinusoidal background magnetic field gradient of wavelength λ and maximum internal gradient strength g . The blue dashed line corresponds to the magnetization averaged with the effective internal gradient distribution in the right insets using the internal gradient ensemble model. The red dotted line shows the signal decay only due to the spin interaction with the applied gradient. The yellow solid line is the signal decay derived from the IGDT expansion of Eq. (33), evaluated with the moments of the effective gradient distribution of the right insets. The free diffusion coefficient is $D_0 = 2 \mu\text{m}^2/\text{ms}$ and the diffusion correlation time $\tau_c = 10$ ms (associated with a restriction length $l_c = \sqrt{D_0\tau_c} = 4.47 \mu\text{m}$). Four conditions are shown: (a) free diffusion regime with $\lambda = 30l_c$, $g = 1000$ mT/m and an applied gradient $G = 3000$ mT/m; (b) restricted diffusion regime with $\lambda = 50l_c$, $g = 30$ mT/m and $G = 100$ mT/m; (c) free diffusion regime with $\lambda = 3l_c$, $g = 1200$ mT/m and $G = 3000$ mT/m and (d) restricted diffusion regime with $\lambda = 3l_c$, $g = 100$ mT/m and $G = 100$ mT/m.

analytic continuation of Eq. (4) in the complex domain. Then, if the standard deviation of the internal gradient distribution is too high (for example > 500 mT/m in our simulations) the IGDT expansion would be only valid at short times within the free diffusion regimen as shown in Fig. 9a and c.

7. CONCLUSIONS

Diffusion processes in disordered systems are of great interest in several areas as physics, biology and medicine, however they are very complex to characterize. In

this article, we exploit the diffusion of spin-bearing particles to probe magnetic field inhomogeneities that contain information about the media microstructure heterogeneities. We consider internal gradients induced by magnetic susceptibility heterogeneity that depend on the morphological information of the media. The spin-bearing particles diffuse within them and probe the effective gradients seen along their movement. We introduced a model that simplifies the naturally complex problem to an ensemble of spatially constant internal gradients that defines a distribution that can be characterized by its first moments. We demonstrate that this gradient ensemble approximation is useful as the

gradients explored by the spin-bearing particles remains close to the real distribution in general, as in expected realistic conditions. We demonstrate that the diffusion process in an inhomogeneous field produces a motional average of the gradient seen by the spins, thus narrowing the effective internal gradient distribution. We also show that the spin magnetization decay is well characterized by only the moments of the effective internal gradient distribution.

This internal gradient ensemble model allows a spin phase's cumulant expansion decomposition for the magnetization signal decay. Based on this cumulant expansion framework, we derive an IGDT-expansion that provides the moments of the internal gradient distributions. The IGDT contains information about the anisotropies of the internal gradient distributions that intrinsically depends on the susceptibility heterogeneity of the media and its orientation with respect to the static magnetic field. Each IGDT term provides different information about the internal gradient distribution.

The IGDT effects may be weak in some scenarios, thus exploiting the presented framework, we propose modulated gradient spin echo sequences to enhance those effects. The enhancement strategy is based on smooth applied gradient modulations and a suitable timing interplay between the time modulating symmetries of the applied and internal gradients. We identify four groups of terms of the IGDT expansion that can be measured independently by a suitable design of the pulse sequence using multiple applied gradient directions in a similar vein as DTI is estimated. We demonstrate the feasibility of the implementation of this framework to measure IGDT terms from the magnetization signal decay in free and restricted diffusion regimes using typical brain tissue conditions. We also evaluate the validity of the model to represent the real distribution convoluted with the molecular diffusion process, and show the regimes where the model can be suitably used. We also discussed some limitations of the model.

We observed that the effective internal gradient distribution reproduces well the real one when the diffusion is either free or the characteristic length of the internal gradients spatial variations is small compared with the diffusion length of the spin-bearing particles. However, in the restricted diffusion regime, the internal local gradients might be averaged by the molecular motion, thus losing information about their distribution. We thus expect the proposed IGDT method to be useful to monitor extra-axonal diffusion, since characteristic length might be wider than in the intra-axonal regions, thus allowing to extend the free diffusion time to probe smooth internal gradient variations [63].

As brain physiology is regulated by molecules and structures as the myelin sheath of axons with significant magnetic susceptibility in comparison with the surrounding medium, the degree of axon myelination significantly affects the internal gradient distributions [25, 56, 63, 103]. Thus internal gradient distributions

show correlations with the amount of myelin in tissues as potential biomarkers for many degenerative diseases. Our results thus contribute to estimate IGDT in this situations that may be especially useful for unveiling structures and fiber orientation based on these susceptibility induced changes [29, 30, 62, 63]. The IGDT are complementary to DTI as they may estimate anisotropies when diffusion is free or isotropic [24, 30, 63].

DECLARATION OF INTERESTS

The authors declare that they have no known competing financial interests or personal relationships that could have appeared to influence the work reported in this paper.

ACKNOWLEDGMENTS

We thank Melisa Gimenez and Martin Kuffer for reading the article and for their suggestions to improve the writing, and to Manuel O. Caceres for the fruitful discussions. This work was supported by CNEA; CONICET; ANPCyT-FONCyT PICT-2017-3156, PICT-2017-3699, PICT-2018-4333, PICT-2021-GRF-TI-00134, PICT-2021-I-A-00070; PIP-CONICET (11220170100486CO); UNCUIYO SIIP Tipo I 2019-C028, 2022-C002, 2022-C030; Instituto Balseiro; A collaboration program from MINCYT (Argentina) and MAECI (Italy) and Erasmus+ Higher Education program from the European Commission between the CIMEC (University of Trento) and the Instituto Balseiro (Universidad Nacional de Cuyo).

Appendix A: General demonstration of the proposed sequence design conditions defines $|\beta^{0G}(t_d) - \beta^{GG}(t_d)|$ positive-definite

We show in Sec. 4.2 of the main text, a necessary relation between the overlap matrices β^{GG} and β^{0G} that have to be fulfilled for enhancing the cross term contributions in Eq. (15). Thus the relation we derive is a necessary condition, since there are other factors that control the intensity of these terms such as the angle between the applied and mean background gradient or even the applied gradient strength. Considering the first two terms $\frac{1}{2}G_i\beta_{ij}^{GG}(t)G_j$ and $G_i\beta_{ij}^{0G}(t)\langle G_0 \rangle_j$ in Eq. (15), we require

$$\left| \mathbf{n} \cdot \beta^{0G} \cdot \mathbf{n} \right| > \mathbf{n} \cdot \beta^{GG} \cdot \mathbf{n} \quad (\text{A1})$$

for the matrix elements in an arbitrary n direction, to enhance the weight of the second term compared to the first one. We thus focus on the maximization of the cross terms overlap matrices β^{0G} . In the principal axes of

the matrices β^{GG} and β^{0G} , the matrix element can be written as

$$\left| \mathbf{n} \cdot \beta^{0G} \cdot \mathbf{n} \right| = \left| \sum_j (\tilde{n}_j)^2 \beta_j^{0G} \right| \leq \sum_j (\tilde{n}_j)^2 |\beta_j^{0G}|,$$

where \tilde{n}_j are the components of the unit vector \mathbf{n} in the overlap matrices eigenbasis. Thus requiring the condition $\mathbf{n} \cdot \beta^{0G} \cdot \mathbf{n} > \mathbf{n} \cdot \beta^{GG} \cdot \mathbf{n}$ is equivalent to request $|\beta^{0G}(t_d)| - \beta^{GG}(t_d)$ to be positive-definite.

In section 4.2, we derived general conditions that the gradient control sequences have to fulfill in order to satisfy (20). That is: *i*) the background gradient modulation $f_0(t)$ has to be an even function with respect to $t_d/2$ with a minimal number of pulses; *ii*) the applied gradient modulation has to be an MGSE sequence with a smooth modulation function ($|f_G(t)| \leq 1$), with a single refocusing echo matching the zero crossing time with a π -pulse that modulate $f_0(t)$ and *iii*) the modulation function $f_G(t)$ has to be an odd function with respect to its middle time, *i.e.* the zero crossing time, and should vanish also at every π -pulse that modulate $f_0(t)$. These conditions ensure that the effective interaction times defined in Eqs. (22) and (23) satisfy $T_{0G} > T_G$. Moreover, if ω_0 is the frequency at the highest pick of the cross modulation filter and ω_G the frequency at the maximum applied gradient filter, the above conditions also ensure $\omega_G > \omega_0$.

The filters in the overlap integrals in Eqs. (7) and (9) have a bandwidth around the frequencies ω_G and ω_0 , respectively. If the filter bandwidths are small compared with the spectral density width, we can factor out from the integral the noise spectral density at the filter frequency, since it is approximately constant within the filter bandwidth. Then, Eqs. (7) and (9) can be approximated by $\beta^{GG}(t_d) \approx \gamma^2 \mathcal{S}(\omega_G) T_G$ and $\beta^{0G}(t_d) \approx \gamma^2 \mathcal{S}(\omega_0) T_{0G}$, respectively. If not, we can roughly hold this approximation, since we can take the constant $\mathcal{S}(\omega^*)$ out from the integral, with ω^* belonging to the filter bandwidth and $\omega^* \approx \omega_G$ and $\omega^* \approx \omega_0$ respectively. Here, the diffusion time t_d dependence is encoded in the effective interactions times and gradient modulation frequencies. Generally, the eigenvalues $S(\omega)$ of the spectral density are monotonically decreasing functions of ω with a maximum at zero frequency. Then, since $\omega_G > \omega_0$ and $T_{0G} > T_G$, $|\beta^{0G}(t_d)| - \beta^{GG}(t_d)$ is positive-definite.

Appendix B: Enhancing the cross-filter overlap with the diffusion spectral density

In section 4.2, we derive the conditions that gradient modulation sequences have to fulfill to guarantee the matrix $|\beta^{0G}(t_d)| - \beta^{GG}(t_d)$ to be positive-definite. This condition is ensured by making the effective

interaction times of gradients with the diffusing spin-bearing particles defined in Eqs. (22, 23) to satisfy $T_{0G} > T_G$. This condition is achieved by making $f_0(t)f_G(t) = |f_G(t)|$.

We thus aim to maximize the eigenvalues of the matrix $|\beta^{0G}(t_d)| - \beta^{GG}(t_d)$. For that, we maximize the lowest frequency peak of the cross-filter $\Re [F_0(\omega, t_d) F_G^*(\omega, t_d)]$. In principle, the condition $f_0(t)f_G(t) = |f_G(t)|$ and the maximization of the low frequency peak of the cross-filter are independents, and might not be satisfied simultaneously. Here we demonstrate that, in fact, both condition could be satisfied at the same time.

First we evaluate the condition for the time-shift of the applied gradient modulation for the asymmetric sequence that maximize *the cross-term* overlap contribution. This time-shift maximizes the cross-filter at the background gradient modulation frequency in order to optimize the overlap with the displacement spectral density $\mathcal{S}(\omega)$. The cross-filter can be written as

$$\Re [F_0(\omega) F_G^*(\omega)] = \tilde{F}_0(\omega) \tilde{F}_G(\omega) \cos [\omega \Delta t - \pi/2] \quad (\text{B1})$$

assuming an arbitrary time-shift Δt , where $\tilde{F}_0(\omega)$ and $\tilde{F}_G(\omega)$ are real functions corresponding to the Fourier transform of the gradient modulations centered at $t = 0$. The phase shift in $\pi/2$ comes from the fact that we consider the applied gradient modulation as an odd function. Here we omit the diffusion time t_d dependence of the Fourier transform in order to simplify the notation. Let be ω_0 the principal harmonic frequency of the background gradient modulation $f_0(t)$. For the two pulse CPMG sequence, the main harmonic is $\omega_0 \approx 2\pi/t_d$. To optimize the cross-filter of Eq. (B1), we require that

$$\omega_0 \Delta t - \pi/2 = n\pi$$

with $|n| = 0, 1, 2, \dots$. Then, the optimal time-shift is

$$\Delta t = \frac{\pi}{\omega_0} (n + 1/2). \quad (\text{B2})$$

There are two solution with n such that $\Delta t < t_d/2$ which give $\Delta t = \pm t_d/4$. These time shifts synchronize exactly the zero crossing time of $f_G(t)$ with the times when the RF π -pulse are applied in the two pulse CPMG sequence.

This optimization is useful as long as $|\tilde{F}_0(\omega_0)| > |\tilde{F}_G(\omega_0)| > 0$. The first relation is always true by construction and the second one impose a restriction on how high can be the frequency with which can be modulated the applied gradient. Thus we show how both requirements to enhance the background gradient effect, the effective interaction times relation $T_{0G} > T_G$ and the low frequency filtering of the cross modulation, can be optimized simultaneously.

Appendix C: General filters and overlap functions

In this section we provide the exact expression for the filters of the GDGSE modulation, a two-pulses CPMG sequence modulation, and the cross filter

$\Re [F_0(\omega, t_d)F_G^*(\omega, t_d)]$ that appear in Eqs. (7-9) in the main text. We consider the gradients modulations independent of the applied gradient direction. We also provide the exact analytic expressions for the corresponding overlap functions for one dimensional diffusion. The filter function for the two pulse CPMG sequence of the background gradient modulation is

$$|F_0(\omega, t_d)|^2 = \frac{256}{\omega^2} \cos^2\left(\frac{t_d\omega}{8}\right) \sin^6\left(\frac{t_d\omega}{8}\right). \quad (\text{C1})$$

The Fourier transform of the GDGSE modulation is

$$F_G(\omega, t_d) = i\sqrt{2\pi e}\alpha^2 t_d^2 \omega e^{i\frac{T}{2}\omega} e^{-\frac{\alpha^2 t_d^2}{2}\omega^2} \quad (\text{C2})$$

and thus its filter function is

$$|F_G(\omega, t_d)|^2 = 2\pi e\alpha^4 t_d^4 \omega^2 e^{-\alpha^2 t_d^2 \omega^2}. \quad (\text{C3})$$

The cross-filter is

$$\begin{aligned} \Re [F_0(\omega, t_d)F_G^*(\omega, t_d)] &= 32\sqrt{2\pi e}\alpha^2 t_d^2 e^{-\frac{\alpha^2 t_d^2}{2}\omega^2} \\ &\times \cos^2\left(\frac{t_d\omega}{8}\right) \sin^4\left(\frac{t_d\omega}{8}\right). \end{aligned} \quad (\text{C4})$$

With these filters and considering the diffusion spectral density

$$S(\omega) = 2D_0 (\tau_c^{-2} + \omega^2)^{-1},$$

we determine the overlap functions using Eqs. (7-9) in the main text

$$\begin{aligned} \beta^{GG}(t_d) &= 2\gamma^2 D_0 \sqrt{\pi e} \alpha^3 t_d^3 \\ &\times \left[1 - \frac{\sqrt{\pi} \alpha t_d}{\tau_c} e^{\frac{\alpha^2 t_d^2}{\tau_c^2}} \operatorname{erfc}\left(\frac{\alpha t_d}{\tau_c}\right) \right], \end{aligned} \quad (\text{C5})$$

$$\begin{aligned} \beta^{00}(t_d) &= 2\gamma^2 D_0 \tau_c^3 \left(\frac{t_d}{\tau_c} - 5 + e^{-\frac{t_d}{\tau_c}} - 4e^{-\frac{3t_d}{4\tau_c}} \right. \\ &\quad \left. + 4e^{-\frac{t_d}{2\tau_c}} + 4e^{-\frac{t_d}{4\tau_c}} \right), \end{aligned} \quad (\text{C6})$$

and

$$\begin{aligned} \beta^{0G}(t_d) &= \gamma^2 D_0 \sqrt{\frac{\pi e}{2}} \tau_c \alpha^2 t_d^2 e^{\frac{\alpha^2 t_d^2}{2\tau_c^2}} \left[4\operatorname{erfc}\left(\frac{\alpha t_d}{\sqrt{2}\tau_c}\right) \right. \\ &\quad - 2e^{\frac{t_d}{2\tau_c}} \operatorname{erfc}\left(\frac{\alpha t_d/\tau_c + 1/(2\alpha)}{\sqrt{2}}\right) \\ &\quad - 2e^{-\frac{T}{2\tau_c}} \operatorname{erfc}\left(\frac{\alpha t_d/\tau_c - 1/(2\alpha)}{\sqrt{2}}\right) \\ &\quad - e^{\frac{t_d}{4\tau_c}} \operatorname{erfc}\left(\frac{\alpha T/\tau_c + 1/(4\alpha)}{\sqrt{2}}\right) \\ &\quad - e^{-\frac{t_d}{4\tau_c}} \operatorname{erfc}\left(\frac{\alpha t_d/\tau_c - 1/(4\alpha)}{\sqrt{2}}\right) \\ &\quad + e^{\frac{3t_d}{4\tau_c}} \operatorname{erfc}\left(\frac{\alpha t_d/\tau_c + 3/(4\alpha)}{\sqrt{2}}\right) \\ &\quad \left. + e^{-\frac{3t_d}{4\tau_c}} \operatorname{erfc}\left(\frac{\alpha t_d/\tau_c - 3/(4\alpha)}{\sqrt{2}}\right) \right]. \end{aligned} \quad (\text{C7})$$

Here, $\operatorname{erfc}(x)$ denote the complementary error function. The generalization to a three-dimensional diffusion is made by considering the correlation time τ_c as a rank 3 tensor, whose eigenvalues are the correlation times in its principal directions, as is shown in Fig 3 of the main text.

-
- [1] P. T. Callaghan, J. Stepišnik, Frequency-domain analysis of spin motion using modulated-gradient NMR, *J. Magn. Reson. A* 117 (1) (1995) 118. [doi:10.1006/jmra.1995.9959](https://doi.org/10.1006/jmra.1995.9959).
- [2] L. Latour, R. Kleinberg, P. Mitra, C. Sotak, Pore-size distributions and tortuosity in heterogeneous porous media, *J. Magn. Reson. A* 112 (1) (1995) 83–91. [doi:10.1006/jmra.1995.1012](https://doi.org/10.1006/jmra.1995.1012).
- [3] J. Stepišnik, S. Lasič, A. Mohorič, I. Serša, A. Sepe, Spectral characterization of diffusion in porous media by the modulated gradient spin echo with CPMG sequence, *J. Magn. Reson.* 182 (2) (2006) 195. [doi:10.1016/j.jmr.2006.06.023](https://doi.org/10.1016/j.jmr.2006.06.023).
- [4] Y. Assaf, T. Blumenfeld-Katzir, Y. Yovel, P. J. Basser, Axciliber: a method for measuring axon diameter distribution from diffusion mri, *Magn. Reson. Med.* 59 (6) (2008) 1347–1354. [doi:10.1002/mrm.21577](https://doi.org/10.1002/mrm.21577).
- [5] J. C. Gore, J. Xu, D. C. Colvin, T. E. Yankeelov, E. C. Parsons, M. D. Does, Characterization of tissue structure at varying length scales using temporal diffusion spectroscopy, *NMR Biomed.* 23 (7) (2010) 745. [doi:10.1002/nbm.1531](https://doi.org/10.1002/nbm.1531).
- [6] H. H. Ong, F. W. Wehrli, Quantifying axon diameter and intra-cellular volume fraction in excised mouse spinal cord with q-space imaging, *NeuroImage* 51 (4) (2010) 1360–1366. [doi:10.1016/j.neuroimage.2010.03.063](https://doi.org/10.1016/j.neuroimage.2010.03.063).
- [7] M. E. Komlosh, E. Özarlan, M. J. Lizak, F. Horkay, V. Schram, N. Shemesh, Y. Cohen, P. J. Basser, Pore diameter mapping using double pulsed-field gradient MRI and its validation using a novel glass capillary array phantom, *J. Magn. Reson.* 208 (1) (2011) 128–135. [doi:10.1016/j.jmr.2010.10.014](https://doi.org/10.1016/j.jmr.2010.10.014).
- [8] N. Shemesh, G. A. Álvarez, L. Frydman, Measuring small compartment dimensions by probing diffusion dynamics via non-uniform oscillating-gradient spin-echo (NOGSE) NMR, *J. Magn. Reson.* 237 (2013) 49. [doi:10.1016/j.jmr.2013.09.009](https://doi.org/10.1016/j.jmr.2013.09.009).

- [9] J. Xu, H. Li, K. D. Harkins, X. Jiang, J. Xie, H. Kang, M. D. Does, J. C. Gore, Mapping mean axon diameter and axonal volume fraction by mri using temporal diffusion spectroscopy, *Neuroimage* 103 (2014) 10–19. doi:10.1016/j.neuroimage.2014.09.006.
- [10] N. Shemesh, G. A. Álvarez, L. Frydman, Size distribution imaging by non-uniform oscillating-gradient spin echo (nogse) mri, *PLOS ONE* 10 (7) (2015) e0133201. doi:10.1371/journal.pone.0133201.
- [11] I. Drobnjak, H. Zhang, A. Ianuş, E. Kaden, D. C. Alexander, PGSE, OGSE, and sensitivity to axon diameter in diffusion MRI: Insight from a simulation study, *Magn. Reson. Med.* 75 (2) (2015) 688–700. doi:10.1002/mrm.25631.
- [12] M. Palombo, C. Ligneul, C. Najac, J. L. Douce, J. Flament, C. Escartin, P. Hantraye, E. Brouillet, G. Bonvento, J. Valette, New paradigm to assess brain cell morphology by diffusion-weighted MR spectroscopy in vivo, *Proc. Natl. Acad. Sci. U. S. A.* 113 (24) (2016) 6671–6676. doi:10.1073/pnas.1504327113.
- [13] M. Nilsson, S. Lasič, I. Drobnjak, D. Topgaard, C.-F. Westin, Resolution limit of cylinder diameter estimation by diffusion MRI: The impact of gradient waveform and orientation dispersion, *NMR Biomed.* 30 (7) (2017) e3711. doi:10.1002/nbm.3711.
- [14] M. Drake-Pérez, J. Boto, A. Fitsiori, K. Lovblad, M. I. Vargas, Clinical applications of diffusion weighted imaging in neuroradiology, *Insights Imaging* 9 (4) (2018) 535–547. doi:10.1007/s13244-018-0624-3.
- [15] D. S. Novikov, E. Fieremans, S. N. Jespersen, V. G. Kiselev, Quantifying brain microstructure with diffusion MRI: Theory and parameter estimation, *NMR Biomed.* 32 (4). doi:10.1002/nbm.3998.
- [16] D. S. Novikov, J. Veraart, I. O. Jelescu, E. Fieremans, Rotationally-invariant mapping of scalar and orientational metrics of neuronal microstructure with diffusion MRI, *NeuroImage* 174 (2018) 518–538. doi:10.1016/j.neuroimage.2018.03.006.
- [17] J. Xu, X. Jiang, H. Li, L. R. Arlinghaus, E. T. McKinley, S. P. Devan, B. M. Hardy, J. Xie, H. Kang, A. B. Chakravarthy, J. C. Gore, Magnetic resonance imaging of mean cell size in human breast tumors, *Magn. Reson. Med.* 83 (6) (2019) 2002–2014. doi:10.1002/mrm.28056.
- [18] S. Y. Huang, Q. Tian, Q. Fan, Q. Fan, T. Witzel, B. Wichtmann, J. A. McNab, J. Daniel Bireley, N. Machado, E. C. Klawiter, C. Mekkaoui, L. L. Wald, A. Nummenmaa, High-gradient diffusion MRI reveals distinct estimates of axon diameter index within different white matter tracts in the in vivo human brain, *Brain Struct. Funct.* 225 (4) (2020) 1277–1291. doi:10.1007/s00429-019-01961-2.
- [19] J. Veraart, D. Nunes, U. Rudrapatna, E. Fieremans, D. K. Jones, D. S. Novikov, N. Shemesh, Noninvasive quantification of axon radii using diffusion MRI, *eLife* 9. doi:10.7554/eLife.49855.
- [20] M. Palombo, A. Ianus, M. Guerrerri, D. Nunes, D. C. Alexander, N. Shemesh, H. Zhang, SANDI: A compartment-based model for non-invasive apparent soma and neurite imaging by diffusion MRI, *NeuroImage* 215 (2020) 116835. doi:10.1016/j.neuroimage.2020.116835.
- [21] M. Capigliani, A. Zwick, P. Jiménez, G. A. Álvarez, Noninvasive quantitative imaging of selective microstructure sizes via magnetic resonance, *Phys. Rev. Applied* 15 (2021) 014045. doi:10.1103/PhysRevApplied.15.014045.
- [22] M. D. Hürlimann, Effective gradients in porous media due to susceptibility differences, *J. Magn. Reson.* 131 (2) (1998) 232–240. doi:10.1006/jmre.1998.1364.
- [23] Y.-Q. Song, Determining pore sizes using an internal magnetic field, *J. Magn. Reson.* 143 (2) (2000) 397–401. doi:10.1006/jmre.1999.2012.
- [24] S. Han, Y. Song, F. Cho, S. Ryu, G. Cho, Y.-Q. Song, H. Cho, Magnetic field anisotropy based MR tractography, *J. Magn. Reson.* 212 (2) (2011) 386–393. doi:10.1016/j.jmr.2011.07.021.
- [25] C. Liu, W. Li, G. A. Johnson, B. Wu, High-field (9.4T) MRI of brain dysmyelination by quantitative mapping of magnetic susceptibility, *Neuroimage* 56 (3) (2011) 930–938. doi:10.1016/j.neuroimage.2011.02.024.
- [26] J. Duyn, MR susceptibility imaging, *J. Magn. Reson.* 229 (2013) 198–207. doi:10.1016/j.jmr.2012.11.013.
- [27] G. A. Álvarez, N. Shemesh, L. Frydman, Diffusion-assisted selective dynamical recoupling: A new approach to measure background gradients in magnetic resonance, *J. Chem. Phys.* 140 (8) (2014) 084205. doi:10.1063/1.4865335.
- [28] Y. Zhang, L. Xiao, G. Liao, B. Blümich, Direct correlation of internal gradients and pore size distributions with low field NMR, *J. Magn. Reson.* 267 (2016) 37–42. doi:10.1016/j.jmr.2016.04.009.
- [29] T. Xu, S. Foxley, M. Kleinnijenhuis, W. C. Chen, K. L. Miller, The effect of realistic geometries on the susceptibility-weighted MR signal in white matter, *Magn. Reson. Med.* 79 (1) (2017) 489–500. doi:10.1002/mrm.26689.
- [30] G. A. Álvarez, N. Shemesh, L. Frydman, Internal gradient distributions: A susceptibility-derived tensor delivering morphologies by magnetic resonance, *Sci. Rep.* 7 (2017) 3311. doi:10.1038/s41598-017-03277-9.
- [31] A. D. Sandgaard, V. G. Kiselev, N. Shemesh, S. N. Jespersen, Incorporating white matter microstructure in the estimation of magnetic susceptibility in ex-vivo mouse brain (2022). doi:10.48550/ARXIV.2208.02594.
- [32] P. T. Callaghan, *Translational Dynamics and Magnetic Resonance: Principles of Pulsed Gradient Spin Echo NMR*, OUP Oxford, 2011.
- [33] C. Messina, R. Bignone, A. Bruno, A. Bruno, F. Bruno, M. Calandri, D. Caruso, P. Coppolino, R. D. Robertis, F. Gentili, I. Grazzini, R. Natella, P. Scalise, A. Barile, R. Grassi, D. A. and, Diffusion-weighted imaging in oncology: An update, *Cancers* 12 (6) (2020) 1493. doi:10.3390/cancers12061493.
- [34] S. Mori, B. J. Crain, V. P. Chacko, P. C. M. Van Zijl, Three-dimensional tracking of axonal projections in the brain by magnetic resonance imaging, *Ann. Neurol.* 45 (2) (1999) 265–269. doi:10.1002/1531-8249(199902)45:2<265::AID-ANA21>3.0.CO;2-3.
- [35] P. J. Basser, J. Mattiello, D. Lebihan, Estimation of the effective self-diffusion tensor from the NMR spin echo, *J. Magn. Reson. B* 103 (3) (1994) 247. doi:10.1006/jmrb.1994.1037.
- [36] P. J. Basser, J. Mattiello, D. Lebihan, MR diffusion tensor spectroscopy and imaging., *Biophys. J.* 66 (1) (1994) 259. doi:10.1016/S0006-3495(94)80775-1.

- [37] P. J. Basser, D. K. Jones, Diffusion-tensor MRI: theory, experimental design and data analysis – a technical review, *NMR Biomed.* 15 (7-8) (2002) 456–467. doi:10.1002/nbm.783.
- [38] D. Le Bihan, J.-F. Mangin, C. Poupon, C. A. Clark, S. Pappata, N. Molko, H. Chabriat, Diffusion tensor imaging: concepts and applications, *J. Magn. Reson. Imaging* 13 (4) (2001) 534–546. doi:10.1002/jmri.1076.
- [39] D. Le Bihan, Looking into the functional architecture of the brain with diffusion MRI, *Nat. Rev. Neurosci.* 4 (6) (2003) 469. doi:10.1038/nrn1119.
- [40] S. Mori, P. C. M. van Zijl, Fiber tracking: principles and strategies – a technical review, *NMR Biomed.* 15 (7-8) (2002) 468–480. doi:10.1002/nbm.781.
- [41] D. K. Jones, A. Simmons, S. C. Williams, M. A. Horsfield, Non-invasive assessment of axonal fiber connectivity in the human brain via diffusion tensor MRI, *Magn. Reson. Med.* 42 (1) (1999) 37–41. doi:10.1002/(sici)1522-2594(199907)42:1<37::aid-mrm7>3.0.co;2-o.
- [42] L. R. Frank, Anisotropy in high angular resolution diffusion-weighted MRI, *Magn. Reson. Med.* 45 (6) (2001) 935–939. doi:10.1002/mrm.1125.
- [43] E. Haacke, J. Patrick, G. Lenz, T. Parrish, The separation of water and lipid components in the presence of field inhomogeneities, *Rev. Magn. Reson. Med.* 1 (2) (1986) 123–54.
- [44] J. Mao, H. Yan, W. Brey, W. Bidgood, J. Steinbach, A. Mancuso, Fat tissue and fat suppression, *Magn. Reson. Imaging* 11 (3) (1993) 385–393. doi:10.1016/0730-725x(93)90071-k.
- [45] L. Axel, Blood flow effects in magnetic resonance imaging., *Magn. Reson. Annu.* (1986) 237–244.
- [46] R. Alfidi, T. Masaryk, E. Haacke, G. Lenz, J. Ross, M. Modic, A. Nelson, J. LiPuma, A. Cohen, MR angiography of peripheral, carotid, and coronary arteries, *Am. J. Roentgenol.* 149 (6) (1987) 1097–1109. doi:10.2214/ajr.149.6.1097.
- [47] J. R. Reichenbach, R. Venkatesan, D. J. Schillinger, D. K. Kido, E. M. Haacke, Small vessels in the human brain: MR venography with deoxyhemoglobin as an intrinsic contrast agent., *Radiology* 204 (1) (1997) 272–277. doi:10.1148/radiology.204.1.9205259.
- [48] J. H. Duyn, P. van Gelderen, T.-Q. Li, J. A. de Zwart, A. P. Koretsky, M. Fukunaga, High-field MRI of brain cortical substructure based on signal phase, *Proc. Natl. Acad. Sci.* 104 (28) (2007) 11796–11801. doi:10.1073/pnas.0610821104.
- [49] S. Eskreis-Winkler, K. Deh, A. Gupta, T. Liu, C. Wisnieff, M. Jin, S. A. Gauthier, Y. Wang, P. Spincemaille, Multiple sclerosis lesion geometry in quantitative susceptibility mapping (QSM) and phase imaging, *J. Magn. Reson. Imaging* 42 (1) (2014) 224–229. doi:10.1002/jmri.24745.
- [50] S. Eskreis-Winkler, Y. Zhang, J. Zhang, Z. Liu, A. Dimov, A. Gupta, Y. Wang, The clinical utility of QSM: disease diagnosis, medical management, and surgical planning, *NMR Biomed.* 30 (4) (2016) e3668. doi:10.1002/nbm.3668.
- [51] C. Wang, A. B. Martins-Bach, F. Alfaro-Almagro, G. Douaud, J. C. Klein, A. Llera, C. Fiscoe, R. Bowtell, L. T. Elliott, S. M. Smith, B. C. Tendler, K. L. Miller, Phenotypic and genetic associations of quantitative magnetic susceptibility in UK biobank brain imaging, *Nat. Neurosci.* 25 (6) (2022) 818–831. doi:10.1038/s41593-022-01074-w.
- [52] T. Liu, P. Spincemaille, L. de Rochefort, B. Kressler, Y. Wang, Calculation of susceptibility through multiple orientation sampling (COSMOS): A method for conditioning the inverse problem from measured magnetic field map to susceptibility source image in MRI, *Magn. Reson. Med.* 61 (1) (2009) 196–204. doi:10.1002/mrm.21828.
- [53] E. M. Haacke, Y. Xu, Y.-C. N. Cheng, J. R. Reichenbach, Susceptibility weighted imaging (SWI), *Magn. Reson. Med.* 52 (3) (2004) 612–618. doi:10.1002/mrm.20198.
- [54] C. Liu, Susceptibility tensor imaging, *Magn. Reson. Med.* 63 (6) (2010) 1471–1477. doi:10.1002/mrm.22482.
- [55] N. Nestle, A. Qadan, P. Galvosas, W. Süß, J. Kärger, PFG NMR and internal magnetic field gradients in plant-based materials, *Magn. Reson. Imaging* 20 (7) (2002) 567–573. doi:10.1016/s0730-725x(02)00529-5.
- [56] J. Lee, K. Shmueli, B.-T. Kang, B. Yao, M. Fukunaga, P. van Gelderen, S. Palumbo, F. Bosetti, A. C. Silva, J. H. Duyn, The contribution of myelin to magnetic susceptibility-weighted contrasts in high-field MRI of the brain, *Neuroimage* 59 (4) (2012) 3967–3975. doi:10.1016/j.neuroimage.2011.10.076.
- [57] H. Liu, M. N. d'Eurydice, S. Obruchkov, P. Galvosas, Determining pore length scales and pore surface relaxivity of rock cores by internal magnetic fields modulation at 2mhz NMR, *J. Magn. Reson.* 246 (2014) 110–118. doi:10.1016/j.jmr.2014.07.005.
- [58] Y.-Q. Song, S. Ryu, P. N. Sen, Determining multiple length scales in rocks, *Nature* 406 (6792) (2000) 178–181. doi:10.1038/35018057.
- [59] Q. Chen, M. K. Gingras, B. J. Balcom, A magnetic resonance study of pore filling processes during spontaneous imbibition in berea sandstone, *J. Chem. Phys.* 119 (18) (2003) 9609–9616. doi:10.1063/1.1615757.
- [60] J.-F. Kuntz, G. Trausch, P. Palmas, P. Mutzenhardt, D. Canet, Diffusive diffraction phenomenon in a porous polymer material observed by NMR using radio-frequency field gradients, *J. Chem. Phys.* 126 (13) (2007) 134904. doi:10.1063/1.2713379.
- [61] H. J. Cho, E. E. Sigmund, Y. Song, Magnetic resonance characterization of porous media using diffusion through internal magnetic fields, *Materials* 5 (12) (2012) 590–616. doi:10.3390/ma5040590.
- [62] W. C. Chen, S. Foxley, K. L. Miller, Detecting microstructural properties of white matter based on compartmentalization of magnetic susceptibility, *NeuroImage* 70 (2013) 1–9. doi:10.1016/j.neuroimage.2012.12.032.
- [63] J. E. Fajardo, G. A. Álvarez, Internal gradient distribution tensors of white matter tracts models, *Proc. Intl. Soc. Mag. Reson. Med.* 13 (29) (2021) 1716.
- [64] H. Cho, S. Ryu, J. Ackerman, Y.-Q. Song, Visualization of inhomogeneous local magnetic field gradient due to susceptibility contrast, *J. Magn. Reson.* 198 (1) (2009) 88–93. doi:10.1016/j.jmr.2009.01.024.
- [65] S. Wharton, R. Bowtell, Whole-brain susceptibility mapping at high field: A comparison of multiple- and

- single-orientation methods, *Neuroimage* 53 (2) (2010) 515. doi:10.1016/j.neuroimage.2010.06.070.
- [66] P. R. Connolly, W. Yan, D. Zhang, M. Mahmoud, M. Verrall, M. Lebedev, S. Iglauer, P. J. Metaxas, E. F. May, M. L. Johns, Simulation and experimental measurements of internal magnetic field gradients and NMR transverse relaxation times (T₂) in sandstone rocks, *Journal of Petroleum Science and Engineering* 175 (2019) 985–997. doi:10.1016/j.petrol.2019.01.036.
- [67] L. de Rochefort, T. Liu, B. Kressler, J. Liu, P. Spincemaille, V. Lebon, J. Wu, Y. Wang, Quantitative susceptibility map reconstruction from MR phase data using bayesian regularization: Validation and application to brain imaging, *Magn. Reson. Med.* 63 (1) (2010) 194. doi:10.1002/mrm.22187.
- [68] P. N. Sen, S. Axelrod, Inhomogeneity in local magnetic field due to susceptibility contrast, *J. Appl. Phys.* 86 (8) (1999) 4548. doi:10.1063/1.371401.
- [69] W. Li, B. Wu, A. V. Avram, C. Liu, Magnetic susceptibility anisotropy of human brain in vivo and its molecular underpinnings, *Neuroimage* 59 (3) (2012) 2088. doi:10.1016/j.neuroimage.2011.10.038.
- [70] E. L. Hahn, Spin echoes, *Phys. Rev.* 80 (1950) 580. doi:10.1103/PhysRev.80.580.
- [71] H. Y. Carr, E. M. Purcell, Effects of diffusion on free precession in nuclear magnetic resonance experiments, *Phys. Rev.* 94 (1954) 630. doi:10.1103/PhysRev.94.630.
- [72] S. Meiboom, D. Gill, Modified spin-echo method for measuring nuclear relaxation times, *Rev. Sci. Instrum.* 29 (8) (1958) 688. arXiv:https://doi.org/10.1063/1.1716296, doi:10.1063/1.1716296.
- [73] E. O. Stejskal, J. E. Tanner, Spin diffusion measurements: Spin echoes in the presence of a time-dependent field gradient, *J. Chem. Phys.* 42 (1) (1965) 288. doi:10.1063/1.1695690.
- [74] D. S. Grebenkov, NMR survey of reflected brownian motion, *Rev. Mod. Phys.* 79 (2007) 1077. doi:10.1103/RevModPhys.79.1077.
- [75] D. K. Jones, *Diffusion MRI*, Oxford University Press, 2010.
- [76] J. Stepišnik, Time-dependent self-diffusion by NMR spin-echo, *Physica B* 183 (4) (1993) 343. doi:10.1016/0921-4526(93)90124-0.
- [77] S. Lasič, J. Stepišnik, A. Mohoric, Displacement power spectrum measurement by CPMG in constant gradient, *J. Magn. Reson.* 182 (2006) 208. doi:10.1016/j.jmr.2006.06.030.
- [78] G. A. Álvarez, N. Shemesh, L. Frydman, Coherent dynamical recoupling of diffusion-driven decoherence in magnetic resonance, *Phys. Rev. Lett.* 111 (2013) 080404. doi:10.1103/PhysRevLett.111.080404.
- [79] J. R. Klauder, P. W. Anderson, Spectral diffusion decay in spin resonance experiments, *Phys. Rev.* 125 (3) (1962) 912. doi:10.1103/PhysRev.125.912.
- [80] J. Stepišnik, Validity limits of gaussian approximation in cumulant expansion for diffusion attenuation of spin echo, *Physica B* 270 (1) (1999) 110. doi:10.1016/S0921-4526(99)00160-X.
- [81] C. H. Ziener, T. Kampf, H.-P. Schlemmer, L. R. Buschle, Spin dephasing in the gaussian local phase approximation, *J. Chem. Phys.* 149 (24) (2018) 244201. doi:10.1063/1.5050065.
- [82] L. T. Rotkopf, E. Wehrse, H.-P. Schlemmer, C. H. Ziener, Gaussian local phase approximation in a cylindrical tissue model, *Front. Phys.* 9. doi:10.3389/fphy.2021.662088.
- [83] R. Kubo, Generalized cumulant expansion method, *J. Phys. Soc. Jpn.* 17 (7) (1962) 1100–1120. doi:10.1143/jpsj.17.1100.
- [84] N. V. Kampen, *Stochastic Processes in Physics and Chemistry*, Elsevier, 2007. doi:10.1016/b978-044452965-7/50006-4.
- [85] G. E. Uhlenbeck, L. S. Ornstein, On the theory of the brownian motion, *Phys. Rev.* 36 (5) (1930) 823–841. doi:10.1103/physrev.36.823.
- [86] M. Kuffer, A. Zwick, G. A. Álvarez, Path integral framework for characterizing and controlling decoherence induced by nonstationary environments on a quantum probe, *PRX Quantum* 3 (2022) 020321. doi:10.1103/PRXQuantum.3.020321.
- [87] R. C. Wayne, R. M. Cotts, Nuclear-magnetic-resonance study of self-diffusion in a bounded medium, *Phys. Rev.* 151 (1966) 264–272. doi:10.1103/PhysRev.151.264.
- [88] B. Robertson, Spin-echo decay of spins diffusing in a bounded region, *Phys. Rev.* 151 (1966) 273–277. doi:10.1103/PhysRev.151.273.
- [89] A. Zwick, D. Suter, G. Kurizki, G. A. Álvarez, Precision limits of tissue microstructure characterization by magnetic resonance imaging, *Phys. Rev. Applied* 14 (2020) 024088. doi:10.1103/PhysRevApplied.14.024088.
- [90] P. Vatiwutipong, N. Phewchean, Alternative way to derive the distribution of the multivariate ornstein–uhlenbeck process, *Adv. Differ. Equ.* 2019. doi:10.1186/s13662-019-2214-1.
- [91] D. L. Bihan, H. Johansen-Berg, Diffusion MRI at 25: Exploring brain tissue structure and function, *NeuroImage* 61 (2) (2012) 324–341. doi:10.1016/j.neuroimage.2011.11.006.
- [92] K. N. Magdoom, M. E. Komlosh, K. Saleem, D. Gasbarra, P. J. Basser, High resolution ex vivo diffusion tensor distribution MRI of neural tissue, *Front. Phys.* 10. doi:10.3389/fphy.2022.807000.
- [93] E. Caruyer, C. Lenglet, G. Sapiro, R. Deriche, Design of multishell sampling schemes with uniform coverage in diffusion MRI, *Magn. Reson. Med.* 69 (6) (2013) 1534–1540. doi:10.1002/mrm.24736.
- [94] R. V. Mulkern, H. Gudbjartsson, C.-F. Westin, H. P. Zengingonul, W. Gartner, C. R. G. Guttman, R. L. Robertson, W. Kyriakos, R. Schwartz, D. Holtzman, F. A. Jolesz, S. E. Maier, Multi-component apparent diffusion coefficients in human brain, *NMR Biomed.* 12 (1) (1999) 51–62. doi:10.1002/(sici)1099-1492(199902)12:1<51::aid-nbm546>3.0.co;2-e.
- [95] S. E. Maier, P. Bogner, G. Bajzik, H. Mamata, Y. Mamata, I. Repa, F. A. Jolesz, R. V. Mulkern, Normal brain and brain tumor: Multicomponent apparent diffusion coefficient line scan imaging, *Radiology* 219 (3) (2001) 842–849. doi:10.1148/radiology.219.3.r01jn02842.
- [96] R. Sener, Diffusion MRI: apparent diffusion coefficient (ADC) values in the normal brain and a classification of brain disorders based on ADC values, *Comput. Med. Imaging Graph.* 25 (4) (2001) 299–326. doi:10.1016/

- s0895-6111(00)00083-5.
- [97] P. Tofts, D. Lloyd, C. Clark, G. Barker, G. Parker, P. McConville, C. Baldock, J. Pope, Test liquids for quantitative MRI measurements of self-diffusion coefficient in vivo, *Magn. Reson. Med.* 43 (3) (2000) 368–374. doi:10.1002/(sici)1522-2594(200003)43:3<368::aid-mrm8>3.0.co;2-b.
- [98] F. S. Mikelberg, S. M. Drance, M. Schulzer, H. M. Yidegiligne, M. M. Weis, The normal human optic nerve: Axon count and axon diameter distribution, *Ophthalmology* 96 (9) (1989) 1325–1328. doi:10.1016/S0161-6420(89)32718-7.
- [99] D. Barazany, P. J. Basser, Y. Assaf, In vivo measurement of axon diameter distribution in the corpus callosum of rat brain, *Brain* 132 (5) (2009) 1210–1220. doi:10.1093/brain/awp042.
- [100] T. Mingasson, T. Duval, N. Stikov, J. Cohen-Adad, *AxonPacking: An open-source software to simulate arrangements of axons in white matter*, *Front. Neuroinf.* 11. doi:10.3389/fninf.2017.00005. URL <https://www.frontiersin.org/articles/10.3389/fninf.2017.00005/full>
- [101] A. P. Pathak, B. D. Ward, K. M. Schmainda, A novel technique for modeling susceptibility-based contrast mechanisms for arbitrary microvascular geometries: The finite perturber method, *NeuroImage* 40 (3) (2008) 1130–1143. doi:10.1016/j.neuroimage.2008.01.022.
- [102] D. Bailes, I. Young, D. Thomas, K. Straughan, G. Bydder, R. Steiner, NMR imaging of the brain using spin-echo sequences, *Clin. Radiol.* 33 (4) (1982) 395–414. doi:10.1016/s0009-9260(82)80307-3.
- [103] B. A. Holland, D. K. Haas, D. Norman, M. Brant-Zawadzki, T. H. Newton, Mri of normal brain maturation., *Am. J. Neuroradiol.* 7 (2) (1986) 201–208.
- [104] J. P. Wansapura, S. K. Holland, R. S. Dunn, W. S. Ball, NMR relaxation times in the human brain at 3.0 tesla, *J. Magn. Reson. Imaging* 9 (4) (1999) 531–538. doi:10.1002/(sici)1522-2586(199904)9:4<531::aid-jmri4>3.0.co;2-l.
- [105] Y.-Q. Song, Using internal magnetic fields to obtain pore size distributions of porous media, *Concepts Magn. Reson.* 18A (2) (2003) 97–110. doi:10.1002/cmr.a.10072.
- [106] V. G. Kiselev, K. A. Il'yasov, Is the “biexponential diffusion” biexponential?, *Magn. Reson. Med.* 57 (3) (2007) 464. doi:10.1002/mrm.21164.